Petroleum Science 20 (2023) 1488–1512

Contents lists available at ScienceDirect

Petroleum Science

journal homepage: www.keaipublishing.com/en/journals/petroleum-science

Original Paper

Microscale crack propagation in shale samples using focused ion beam scanning electron microscopy and three-dimensional numerical modeling

Xin Liu [a], Si-Wei Meng [b, *], Zheng-Zhao Liang [a], Chun'an Tang [a], Jia-Ping Tao [b], Ji-Zhou Tang [c]

[a] State Key Laboratory of Coastal and Offshore Engineering, Dalian University of Technology, Dalian, Liaoning, 116024, China
[b] Research Institute of Petroleum Exploration Development, China National Petroleum Corporation, Beijing, 100083, China
[c] State Key Laboratory of Marine Geology, Tongji University, Shanghai, 200092, China

ARTICLE INFO

Article history:
Received 29 April 2022
Received in revised form
10 October 2022
Accepted 11 October 2022
Available online 15 October 2022

Edited by Jia-Jia Fei and Teng Zhu

Keywords:
FIB-SEM
Digital image processing
Realistic microstructure
3D digital shale fracture process simulation
Pyrite

ABSTRACT

Reliable prediction of the shale fracturing process is a challenging problem in exploiting deep shale oil and gas resources. Complex fracture networks need to be artificially created to employ deep shale oil and gas reserves. Randomly distributed minerals and heterogeneities in shales significantly affect mechanical properties and fracturing behaviors in oil and gas exploitation. Describing the actual microstructure and associated heterogeneities in shales constitutes a significant challenge. The RFPA^{3D} (rock failure process analysis parallel computing program)-based modeling approach is a promising numerical technique due to its unique capability to simulate the fracturing behavior of rocks. To improve traditional numerical technology and study crack propagation in shale on the microscopic scale, a combination of high-precision internal structure detection technology with the RFPA^{3D} numerical simulation method was developed to construct a real mineral structure-based modeling method. First, an improved digital image processing technique was developed to incorporate actual shale microstructures (focused ion beam scanning electron microscopy was used to capture shale microstructure images that reflect the distributions of different minerals) into the numerical model. Second, the effect of mineral inhomogeneity was considered by integrating the mineral statistical model obtained from the mineral nanoindentation experiments into the numerical model. By simulating a shale numerical model in which pyrite particles are wrapped by organic matter, the effects of shale microstructure and applied stress state on microcrack behavior and mechanical properties were investigated and analyzed. In this study, the effect of pyrite particles on fracture propagation was systematically analyzed and summarized for the first time. The results indicate that the distribution of minerals and initial defects dominated the fracture evolution and the failure mode. Cracks are generally initiated and propagated along the boundaries of hard mineral particles such as pyrite or in soft minerals such as organic matter. Locations with collections of hard minerals are more likely to produce complex fractures. This study provides a valuable method for understanding the microfracture behavior of shales.

1. Introduction

Shale is a fine-grained sedimentary rock with a wide distribution and is also a hydrocarbon source rock (Veytskin et al., 2017; Tang et al., 2021; Zhao et al., 2022). It is a natural composite material comprising organic matter, illite, quartz, calcite, feldspar, and other minerals (Goral et al., 2020; Ma et al., 2019; Zhang et al., 2021), and it contains internal defects such as pores and fractures, which are highly inhomogeneous and the main spaces for the storage of shale oil and gas (Tang and Wu, 2018; Yasin et al., 2021; Hu et al., 2022; Wang et al., 2022). The spatial distribution of these components in this multicomponent system is a characteristic of shale that forms during the sedimentary evolution of shale. The

* Corresponding author.
E-mail address: mengsw@petrochina.com.cn (S.-W. Meng).

https://doi.org/10.1016/j.petsci.2022.10.004

complex microstructural features within shale have an important influence on mechanical behavior and simultaneously cause shales to exhibit complex damage processes under external loading (Rickman et al., 2008; Kumar et al., 2012). The micromechanical properties of different mineral fractions determine the macromechanical behavior of shale (Labani and Rezaee, 2015). In addition to the macroscopic stress field, the nonuniform characteristics of the microstructure within shale may also affect the development of hydraulic fractures, resulting in more tortuous hydraulic fracture extension surfaces and more complex damage patterns (Ouchi et al., 2017; Tang et al., 2018; He et al., 2022). That is, the mechanical behavior of rocks and the emergence and expansion of cracks are largely influenced by the fine internal structure of mineral components, geometric arrangement distribution, and so on (Blair and Cook, 1998; Lan et al., 2010). Therefore, the effects of microstructure must be considered when studying the mechanical properties of shale and the process of fracture extension (Yu et al., 2021). Studies of the influence of mineral components, content, and spatial distribution in shale on the mechanical behavior of the medium, microfracture expansion, and damage patterns from a microscopic perspective are of great theoretical significance for the design of shale oil and gas reservoir extraction processes (Tang et al., 2019a, 2019b).

Many scholars have investigated the mechanical behavior of rocks at the microscopic scale using different micromechanical testing techniques. Veytskin et al. (2017) combined nanoindentation and SEM-EDS to evaluate the relationships between microstructure, mineralogy, and fundamental material properties for a variety of shales with varying textures and mineralogy. Akono and Kabir (2016) studied the fracture properties of organic-rich shale at the microscopic scale by combining advanced imaging techniques, fracture mechanics, and microscale scratch testing methods. Their research provided elastic mechanical parameters such as the elastic modulus and stiffness of microscale shale but could not provide another necessary mechanical parameter, i.e., strength. Given this, to obtain complete mechanical parameters of rock materials, Goral et al. (2020) investigated micromechanical properties at the micron scale by shale micro compression testing using Woodford Shale as an example. Scholars have performed considerable work to obtain the micromechanical properties of rocks (Sone and Zoback, 2013; Bennett et al., 2015; Kumar et al., 2015; Veytskin et al., 2017). However, common micromechanical testing techniques, such as indentation, scratch experiments, and micrometer column experiments, make observation of the crack extension process difficult. Zhao and Zhang (2020) used micromachining methods to fabricate microcantilever beams and performed *in situ* fracture experiments under scanning electron microscopy to study crack extension. The process of crack extension in shale was characterized at the microscale. However, due to the opaqueness of the rock microstructure, this study observed only the crack extension process on the surface and could not observe the details of the process inside the shale.

Although certain nondestructive testing methods, such as computed tomography, may identify interior rock defects without damaging the specimen, distinguishing among various component minerals and monitoring the microfracture process in real time is challenging (Ren and Ge, 2004). Numerical approaches have proven to be a viable alternative as computer technology has advanced, and they are now commonly utilized to analyze the mechanical behavior of rocks and damage processes. Numerical approaches replicate the experimental procedure, and they can also capture the progression of fractures (Wu et al., 2020). Tang (1997, 2000a, 2000b) introduced nonhomogeneous coefficients into the numerical model to represent the nonhomogeneous features of rock materials, and their approach assumed that the mechanical properties of rock materials followed the Weibull distribution. The microstructures of minerals were considered in their analysis, which constitutes a flaw. Liu et al. (2018) approximated the characterization of mineral grains by defining the particle size distribution and size of the Voronoi elements to consider the rock microstructure in the numerical model. However, the random parameters used in these investigations were unpredictable, subjective, and highly reliant on statistical distribution parameters, and crack extension paths may also be random due to the random distribution of the components; this means that these numerical models cannot easily characterize the true microstructure of the rock, and the test results may not provide the phenomenological and experimental effects that the researchers expect when designing the tests.

Digital image processing (DIP) technology has been used in numerical modeling methods for a more realistic reconstruction of rock microstructures as imaging technology has advanced in recent years. Internal microdefects, mineral components, grain shapes, and rock spatial distributions may be included in numerical models for a more realistic microstructural reconstruction that employs image processing. Yue et al. (2003) used the digital image processing (DIP) method to create a two-dimensional numerical model in which the nonhomogeneous characteristics of the rock microstructure were considered. Zhu et al. (2006) included DIP-based rock heterogeneity and microcracks in 2D numerical code rock failure process analysis (RFPA) and investigated their impact on the progression and hydromechanics of fractured rock damage. Zhang et al. (2019) used digital image processing (DIP) to include an enlarged grain-based model with genuine rock microstructures in the numerical model, and the consequences of early microcracks were investigated by lowering the mechanical properties of interparticle contacts. Furthermore, DIP-based modeling approaches have been used extensively in the investigation of thermal cracking issues and hydrofracturing (Yu et al., 2014; Li et al., 2021). Their findings showed that models that account for true 2D microscopic heterogeneity might better predict the mechanical and fracture responses of rocks.

Due to the complexity of the internal structures of rocks and the difficulty of generating 3D models, the studies above were all 2D numerical simulation studies based on 2D digital images. However, this is incompatible with the real three-dimensional situation and can only depict qualitative mechanical behavior. In view of the above, Yu et al. (2015) created 3D numerical models based on prefracturing the rock to create a jointed rock body and then combined CT scanning with finite element numerical methods to develop a 3D numerical model that accounts for the actual spatial morphology of the joint. Tsafnat et al. (2011) created three-dimensional numerical models of porous coke by considering the actual spatial distributions of pores based on CT scanning technology and finite element numerical methods and calibrated the models experimentally. Zhu et al. (2018) reconstructed 3D numerical models based on X-ray micro-CT replicating internal defects in natural rocks, and their results can be used to study the mechanical and fracture properties of the rocks. The rock samples studied by these scholars were characterized by obvious pore spaces, fractures, and joints, which are easily reconstructed by CT identification. However, CT scans are poorly visualized and severely limited by resolution; defects of sizes smaller than the resolution cannot be identified and are not well differentiated for minerals. As a result, the grayscale histogram for CT images of dense rocks is often single-peaked. In addition, the increase in the number of cells in the 3D numerical model results in a substantial computational burden. As a result, the realism and accuracy of most 3D numerical models are not guaranteed due to forced reductions in the number of cells; i.e., the resolution of the image is reduced by a factor of

20–30 or even more during modeling, which leads to a significant reduction in the benefits of numerical modeling methods based on digital images.

In this paper, we propose an RFPA^{3D} microscopic numerical analysis model based on FIB-SEM (focused ion beam-scanning electron microscopy) images that considers the real microstructures of rocks (including the composition and distribution of minerals as well as the internal defects of rocks such as pores and fractures) and investigates the nonlinear mechanical behavior and fracture process of microscopic dense shale (the main research process is shown in Fig. 1). First, FIB-SEM was used to scan the rock samples and obtain clear images of mineral and nanopore structure characteristics. The FIB-SEM images were then processed using the improved digital image processing technique proposed in this paper to better characterize the multicomponent structures of the rocks. Next, the processed FIB-SEM images were imported into the cloud RFPA^{3D} parallel computing program, and a 3D microscopic numerical model characterizing the actual spatial distribution of mineral phases and nanopore structures was established. Furthermore, scanning electron microscopy (SEM) was performed on shale samples under an external force to verify the validity and scientificity of a modeling method based on FIB-SEM and RFPA. Finally, the failure mode, mechanical properties, and crack propagation behavior of microscale shale were explored, and the dynamic

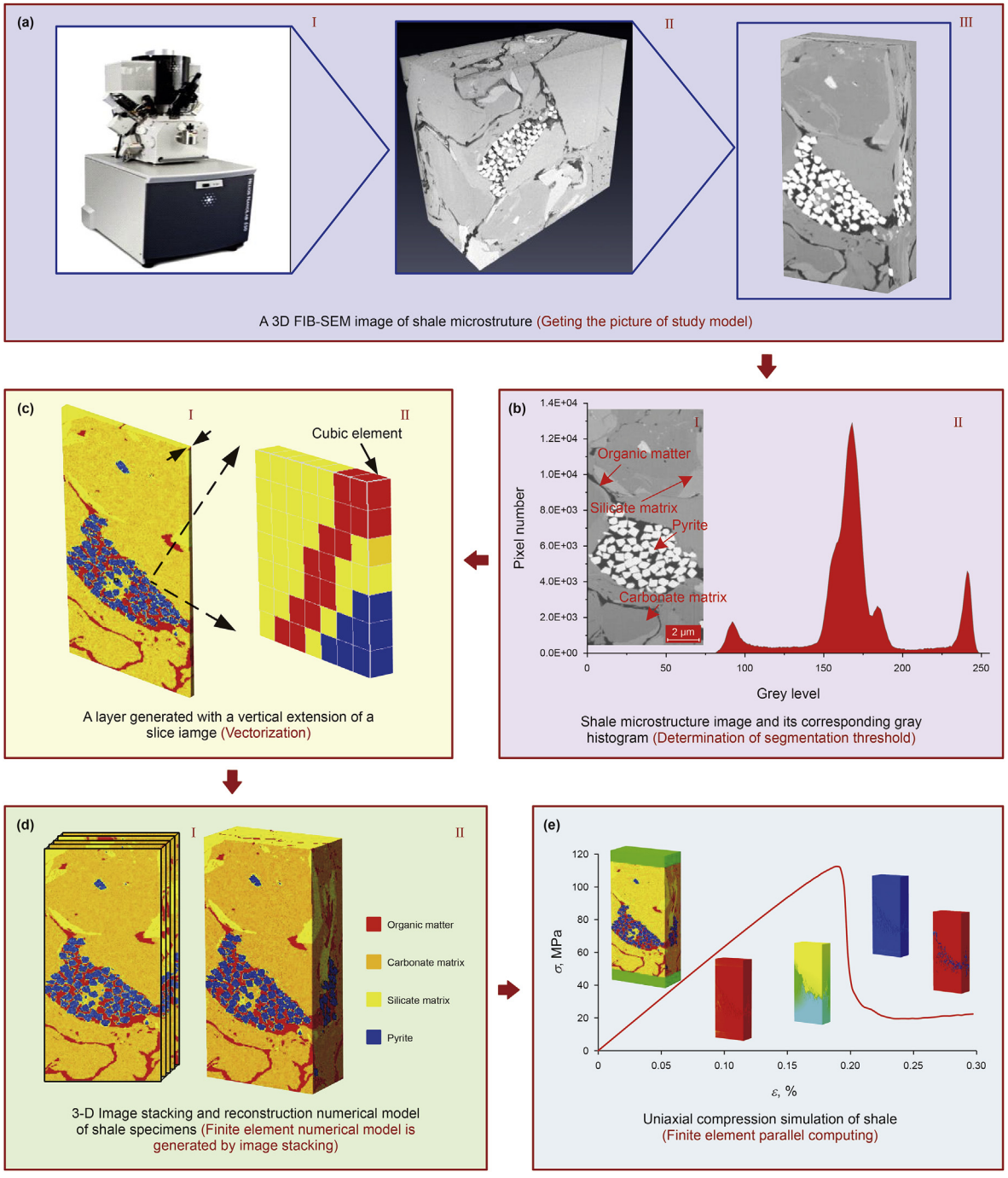

Fig. 1. Digital image processing and numerical simulation of the shale specimen.

microfracture process of samples under uniaxial compressive stress and uniaxial tensile stress was further analyzed by numerical methods, providing a theoretical exploration of the mechanical behavior and fracture mode of shale with microscopic characteristics.

This paper is organized as follows: Sections 2 and 3 describe the FIB-SEM scanning experiments and improved digital image processing techniques used to obtain an actual microstructure of shale samples, respectively. Section 4 introduces the modeling approach based on the combination of FIB-SEM and RFPA. The simulation results and analysis of the results are presented in section 5. The analysis of the SEM images is in section 6, and the discussion and conclusion are presented in sections 7 and 8, respectively.

2. Sample preparation and FIB-SEM scanning

The samples used for the experiments in this chapter were selected from high-maturity pyrite aggregate shales in a shale oil basin in China. First, the samples were cut into suitable slices along the vertical laminar direction with a size of approximately 10 × 10 × 5 mm. Then, mechanical grinding was performed, followed by argon ion polishing. The polished surface was sprayed with a thin layer of gold to increase the electrical conductivity of the sample surface. The processed sample was fixed on the sample stage with conductive adhesive and was processed into a sample as shown in Fig. 2(c) in preparation for the following electron microscopy scanning experiment.

The 3D sectioning and SEM observations of the samples in this section were performed on a FIB-SEM HELIOS NANOLAB650 produced by FEI (Fig. 2(a)). FIB-SEM has been widely used to characterize nanoscale shale structural features (Gu et al., 2015; Tang et al., 2016). Because of the reduced interaction volume, the approach exhibited excellent surface detail and created obvious contrast between pores, organic content, and inorganic minerals in the shale (Curtis et al., 2012). Equipment with a maximum resolution of 0.8 nm, was used to study the microstructures of various shales. The acceleration voltage for SEM was set to 2 keV, the current was set to 0.4 nA, the cutting pitch was set to 10 nm, and the total number of cuts was set to 600. As the particle sizes of shale minerals range from 3.2 to 35 μm (Lei et al., 2015), the resolution used in this research was 20 nm, and the milling pitch was 20 nm, which is sufficient for multicomponent mineral characterization. Sample preparation and FIB-SEM experiments were performed at the Research Institute of Petroleum Exploration and Development of China.

The three-dimensional microstructure of the shale sample is shown in Fig. 3. Both models contained aggregated pyrite particles, but the sizes of pyrite particles in Model 1 were significantly larger than those in Model 2. The single-image resolution for both models was 1024 pixels × 884 pixels. As a total of 256 layers were cut in Model 1, the dimensions of the 3D FIB-SEM images for the shale samples were approximately 20.48 × 17.68 × 5.12 μm. The FIB-SEM image analysis results showed that Model 1 contained three-phase minerals, with white particles representing pyrite, gray minerals representing the carbonate matrix dominated by quartz, and black minerals representing organic matter. A total of 364 layers were cut in Model 2; thus, the dimensions of the 3D FIB-SEM images of the shale samples were approximately 20.48 × 17.68 × 7.28 μm. The results of FIB-SEM image analyses showed that Model 2 contained four-phase minerals, with white particles representing pyrite, light gray minerals representing a silicate matrix dominated by calcite, dark gray minerals representing a carbonate matrix dominated by quartz, and black minerals representing organic matter. In addition, the scanning resolution of Model 1 and Model 2 is the same, and the reason the surface does not appear to be the same size is because of the size of the mineral grains. The pyrite particles in Model 1 are larger than those in Model 2.

3. Realistic multicomponent microstructure characterizations

At the microscopic level, shale is a multicomponent material comprising minerals, such as pyrite, carbonates, silicates, organic matter, and pore spaces. As the purpose of this study was to establish a numerical model that truly reflects the three-dimensional microstructure of shale, various digital image processing techniques were used to process the FIB-SEM images and characterize the three-dimensional real microtopography of shale. Image segmentation is a process of labeling each pixel in an image such that pixels with the same label have common visual properties. In this work, pixels with the same title depict the same mineral fraction, and the purpose of image segmentation is to distinguish the different mineral fractions. Therefore, determining the segmentation threshold is a crucial step in the research process of this study.

3.1. FIB-SEM image analysis

The gray values of different mineral components in shale are different. For example, the gray value of pores is lowest, the gray

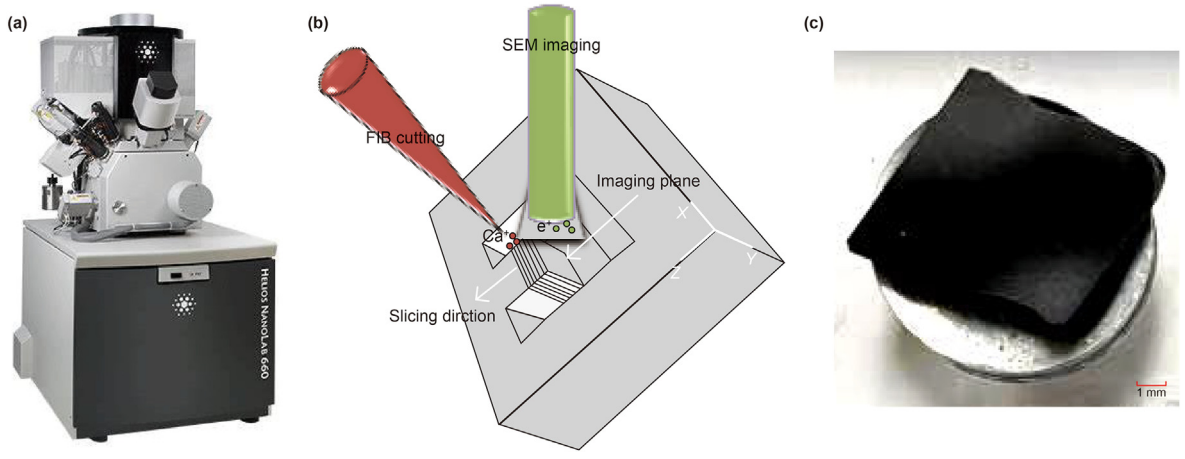

Fig. 2. FIB-SEM instrument and sample; (**a**) FIB-SEM instrumentation, model Helios NanoLab 660; (**b**) pictorial representation of consecutive milling and imaging processes in typical FIB-SEM; and (**c**) sample.

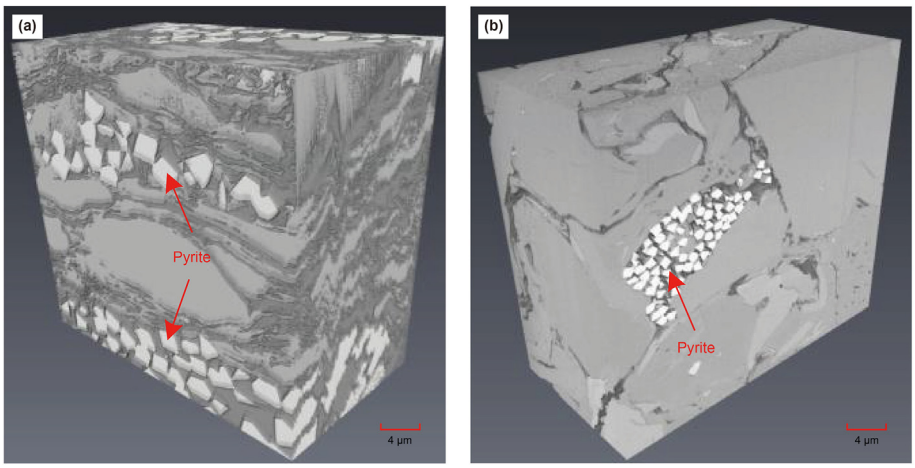

Fig. 3. Three-dimensional FIB-SEM images of shale samples: (**a**) Model 1 and (**b**) Model 2.

value of organic matter is second lowest, the gray value of inorganic minerals is higher, and the gray value of pyrite is the highest. The FIB-SEM image shown in Fig. 4(a) demonstrates the color distribution of multicomponent minerals, i.e., bright objects in the foreground (pyrite), gray areas (carbonate matrix dominated by quartz) and dark areas (organic matter), and it is divided into three-phase minerals. Therefore, the grayscale histogram of this FIB-SEM image should exhibit a bimodal distribution (Yu et al., 2018). However, the histogram shown in Fig. 5 contains multiple peaks and troughs, which means that multiple aggregations of the same gray level are shown in Fig. 4(a). Therefore, the segmentation threshold cannot be determined directly based on this histogram.

FIB-SEM images were selected with four different sets of segmentation thresholds ($T_1 = 59$, $T_2 = 128$; $T_1 = 60$, $T_2 = 120$; $T_1 = 50$, $T_2 = 104$; and $T_1 = 45$, $T_2 = 102$), and the segmentation effects were not ideal. FIB-SEM images segmented with varying thresholds for segmentation, in which pyrite, carbonate matrix, and organic matter are represented by red, green, and blue, respectively, are shown in Fig. 4(b–e). If the threshold was high, the minerals in the upper part of the image were clearly segmented. However, in the lower part of the image, pyrite aggregate particles were mixed with some quartzite, which is obviously undesirable (see Fig. 4(b) and (c)). Conversely, if the threshold was low, the lower part of the image was clearly segmented. However, in the upper part of the image, pyrite was interspersed inside the carbonate, and this result was also clearly unsatisfactory (see Fig. 4(d) and (e)).

In fact, this phenomenon was naturally determined by the principles of FIB-SEM imaging, which was obtained by ion milling (usually with K^+ and Ca^{2+}) and SEM imaging (imaging of sample surfaces using high-energy electron beams). The imaging principle

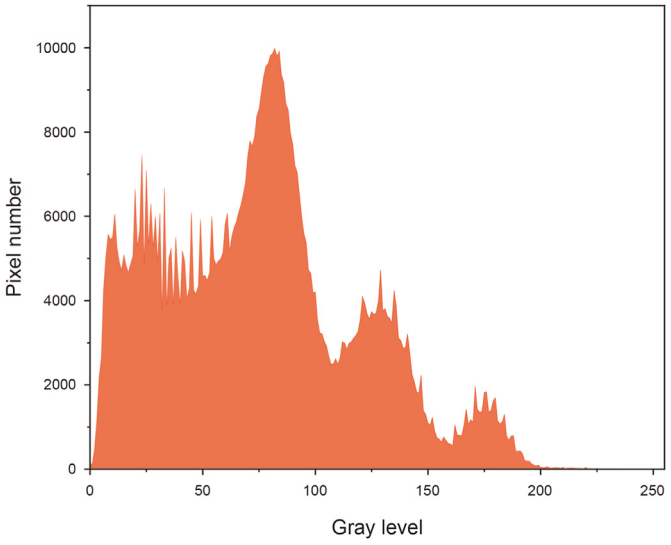

Fig. 5. Gray level histogram of the FIB-SEM image shown in Fig. 4(a).

is shown in Fig. 2(b). The angle between the ion beam and electron beam ranged between 30° and 60° depending on the etching depth (Chandra and Vishal, 2021). Due to the different conductivities of different material elements, the SEM grayscale images showed different brightnesses. Materials with high electrical conductivity emit more energy, making them appear brighter in the SEM images and thus allowing differentiation between mineral classes. Therefore, two main reasons explain the uneven colors of SEM images.

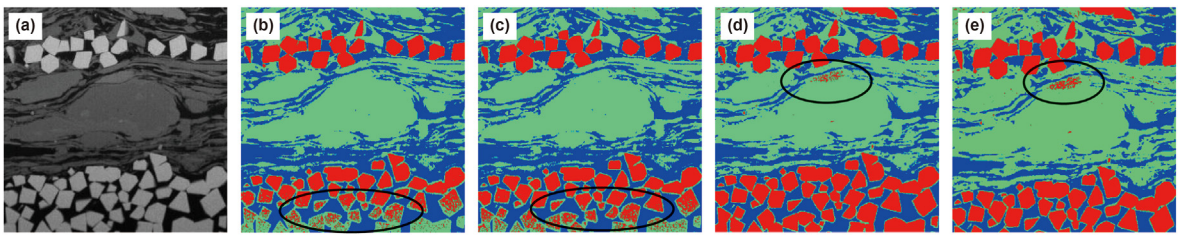

Fig. 4. FIB-SEM multicomponent mineral maps after segmentation using different segment thresholds in which pyrite, carbonate matrix, and organic matter are represented by red, green, and blue, respectively; (**a**) FIB-SEM image. The segment threshold is (**b**) $T_1 = 59$, $T_2 = 128$; (**c**) $T_1 = 60$, $T_2 = 125$; (**d**) $T_1 = 50$, $T_2 = 104$ and (**e**)$T_1 = 45$, $T_2 = 102$ (▪pyrite, ▪carbonate matrix, and ▪organic matter).

One is the instability of the electron beam, and the other is the effect of shielding, which is due to the smaller pit dug during the FIB coarse cutting step; this results in partial signal shielding. In addition, the angle between the electron beam and the ion beam as well as electron beam damage may cause unevenness in the image grayscale. These factors often lead to FIB-SEM images presenting nonuniform color features (bright above and dark below the image), as shown in Fig. 6, and a new threshold segmentation method is needed to address such color features.

3.2. Aggregate characterization

This section proposes an improved segmentation method for characterizing shale microscopy based on the grayscale features of FIB-SEM images. This method extracts some pixels of the whole FIB-SEM image by using rectangles as processing units, and then each part is processed individually with the conventional segmentation method. Assuming that $g(x,y)$ is the gray value of the (x,y) points in the original FIB-SEM image and $f_i(x,y)$ is the gray value of the extracted rectangular image in the original FIB-SEM image, the image is divided into n parts according to the specific situation, and the height of each part of the image is $h_\triangle$, as shown in Fig. 6(c). The extraction process is given by Eq. (1):

$$g(x,y)=\begin{cases} f_1(x,y) & 0 < h_1 \le h_\triangle \\ f_2(x,y) & h_\triangle < h_2 \le 2h_\triangle \\ \cdots \quad \cdots & \\ f_i(x,y) & (i-1)h_\triangle < h_i \le ih_\triangle \\ \cdots \quad \cdots & \\ f_n(x,y) & nh_\triangle < h_n \le h \end{cases} \tag{1}$$

If the total height summation $\sum_{i=1}^{n} h_i$ of the extracted image is greater than the height h of the original FIB-SEM image, the extraction operation is stopped. We selected a FIB-SEM 2D image (Fig. 4(a)) to introduce our proposed improved segmentation method. Parameter $h_\triangle = 200$ pixels (the entire image height is $h =$ 800 pixels), and the rectangular extraction method was used to extract four local images (Fig. 7(a)) from the original image. Note that this is not necessarily an equal height or width extraction. Fig. 7(b) shows the corresponding grayscale histogram for each local image. Clearly, the gray level histograms of Fig. 6(b-I)–(b-III) show three peak distributions with two different trough values. Therefore, the segmentation threshold can be determined according to the histogram. Fig. 7(b-IV) shows the bimodal distribution characteristics. The first trough is a straight-line section, and the specific trough value is difficult to determine. Therefore, this part cannot reasonably be divided into two-phase minerals based on bimodal characteristics. The reason is that according to the enlargement of Fig. 7(a-IV), an obvious excessive interface occurs between pyrite mineral particles and organic matter. The gray value of this interface is between pyrite mineral particles and organic matter, and it is difficult to determine directly from the gray histogram.

Therefore, an automatic method, the Otsu multithreshold segmentation method (Ren et al., 2003), was adopted for the extraction process. Assuming that the gray level of the image is L, the range of gray levels is $[0,1,\cdots,L-1]$. $n-1$ thresholds $T_1, T_2, \cdots T_{n-1}$ are used, and the images are divided into n categories, which are expressed as $C_0 = \{0,1,\cdots,T_1\}$, $\cdots$, $C_i = \{T_i+1, T_i+2, \cdots, T_{i+1}\}$, $\cdots$ $C_{n-1} = \{T_{n-1}+1, T_{n-1}+2, \cdots, L-1\}$, etc.. The probabilities of each category are $P_0, P_1, \cdots P_{n-1}$, and the means are $\mu_0, \mu_1, \cdots \mu_{n-1}$. The multithreshold segmentation equation is as follows:

$$\{T_1^*, T_2^*, \cdots, T_{n-1}^*\} = \underset{1\le T_1 < \cdots T_{n-1} < L}{\operatorname{argmax}} \left\{ \sum_{i=0}^{n-1} P_i(\mu_i - \mu)^2 \right\} \tag{2}$$

Numerous factors can influence unwanted features (such as stray dots) in the segmented image, including noise introduced during scanning. Therefore, noise points must be removed from FIB-SEM images before using the improved method for image segmentation to facilitate FIB-SEMing. Several reasonably simple but effective methods of enhancing images have been developed, including averaging and low-pass filtering methods. However, sharp edges and other details can be blurred using any of these methods. A median filter method replaces pixel values with the median of neighbors to preserve edges between different parts of an image. Thus, leveraging the median filter, the segmented images are enhanced.

Fig. 8 illustrates the median filter principle. Every pixel is considered in conjunction with the pixel itself (surrounded by the red solid line rectangle) and its neighbors (surrounded by the red dotted line rectangle). A medium kernel is a square $(2R+1)$ by $(2R+1)$, where R is the filter radius (1 pixel, as seen in Fig. 8). The original value of the pixel is replaced by the median value. Essentially, the median value is determined from the window data sorted in ascending order. The filter radius is an essential parameter in controlling how smooth the output image is from the median filter method. A trial-and-error process is required to select the filter radius, and it depends on the sampling granularity and image resolution. As the generated image retains the main features of the specimen, the value is assumed to be reasonable.

The filter radius of this study was 1 pixel, and the final confirmed median filter neighborhood window was 3×3 after a comparative study and analysis. In addition, we developed a computer code combining Eq. (1) and Eq. (2) to automatically, quickly, and in batch complete the processing of image chunking, noise

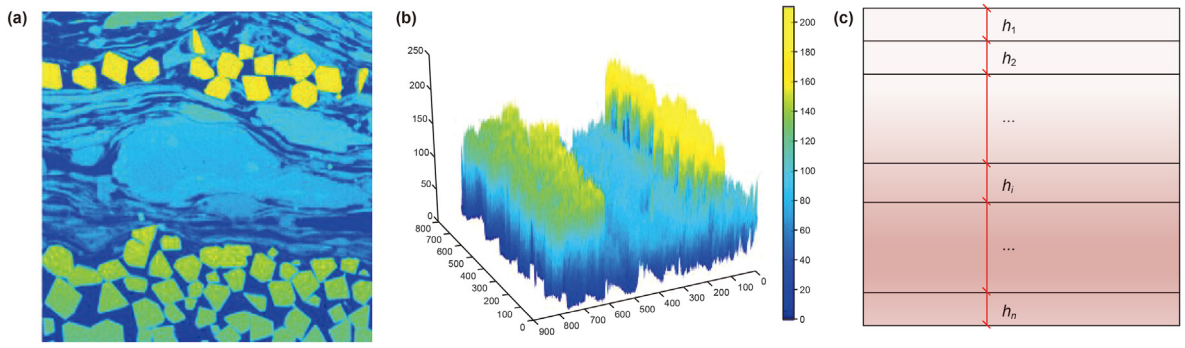

Fig. 6. Color characteristics of FIB-SEM images and segmentation diagram; (**a**) color characteristics of FIB-SEM images; (**b**) FIB-SEM image grayscale distribution in 3D; and (**c**) schematic diagram of inhomogeneous FIB-SEM image segmentation (dark blues represent a gray value of 0, and bright yellow represents a gray value of 255).

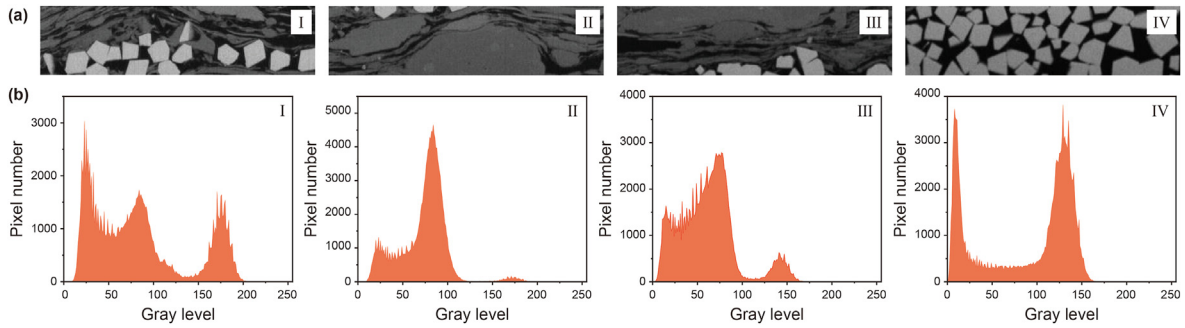

Fig. 7. Partial images and gray-level histograms; (**a**) partial images obtained by rectangle extraction; and (**b**) corresponding gray-level histogram. The segmentation thresholds of I~IV are $T_1 = 59$, $T_2 = 128$; $T_1 = 60$, $T_2 = 125$; $T_1 = 50$, $T_2 = 104$; and $T_1 = 45$, $T_2 = 102$.

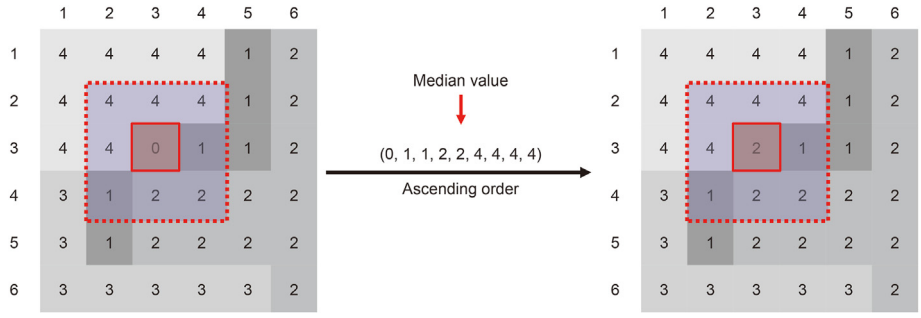

Fig. 8. Application of a median filter to remove stray dots. Each pixel and its eight neighbors are considered for determining the median value due to the filter radius of 1 pixel.

reduction, and segmentation to realistically depict shale microstructures. The output image obtained after image segmentation is shown in Fig. 9. Compared with Fig. 5(a), the distribution of minerals is basically the same as that in the original image. We used a simple and easy method to effectively solve the segmentation problem of inhomogeneous images.

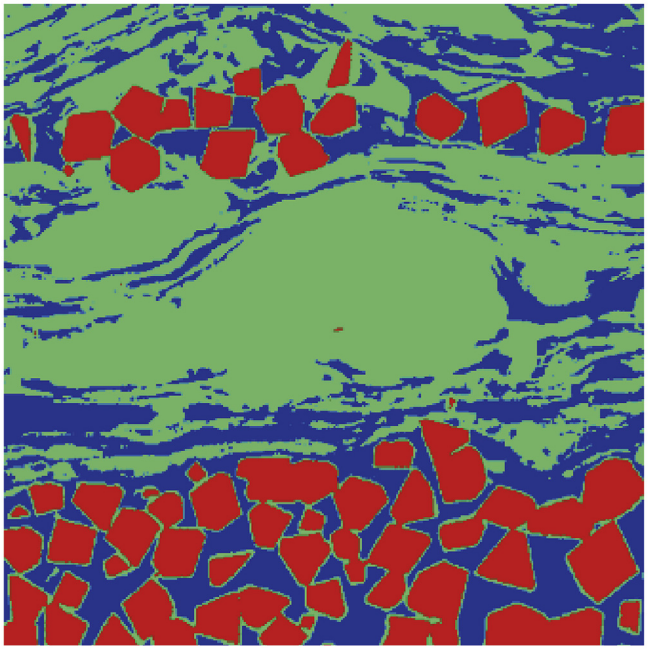

Fig. 9. Image of shale microstructure after segmentation using the improved method (pyrite, carbonate matrix, and organic matter).

4. Numerical model

This subsection aims to build a numerical model based on the actual microstructure and mechanical characteristics and overcome the bottleneck problems of “inaccurate models” and “inaccurate parameters” in previous computational simulations on rocks. The reconstructed numerical model considered the natural mineral structure of the shale and the heterogeneity of the mechanical parameters of the same mineral. Thus, the reconstructed numerical model can more precisely describe the actual microstructure of the rock by incorporating the “double heterogeneity” and “double authenticity” of the structure and material.

4.1. Reconstruction of a realistic shale microstructure numerical model

The microstructural information of the dense shale can be accurately obtained by using the improved digital image processing technique described above and integrated into the RFPA^{3D} numerical model for subsequent simulations. RFPA^{3D} has its own digital image import interface, and the specific numerical model building process includes four steps. First, the FIB-SEM images processed using digital image processing techniques were converted to a 24-bit BMP image format recognizable by RFPA^{3D}, and the images contained information on the microscopic mineral structure of natural shale. Grayscale image information was presented as a data matrix as in Eq. (3), and the matrix value $f(x,y)$ denotes the grayscale value of the image element with data type uint8 and integer values of [0, 255]; second, the single-layer digital image was assumed to have a certain thickness t, as shown in Fig. 1(b), where the FIB-SEM milling thickness $t = 20$ nm. The converted images were stacked layer by layer according to the sequence of FIB-SEM milling to form a three-dimensional microstructure model of shale, as shown in Fig. 1(c). The finite element

mesh was automatically generated at the same time as the 3D model was built. Each finite element cell was a hexahedron. The length and width of the cell were exactly the same depending on the sizes of the image pixels. The thickness of the element was the same as that of milling. The number of cells was determined by the number of pixels, that is, the product of the number of single-layer image pixels and the number of imported FIB-SEM image layers. Then, the segmentation thresholds determined by digital image processing techniques were input into the software, and the reconstructed shale model was divided into multicomponent microstructures, including various types of mineral grains, pores, and fissures. A natural and realistic numerical model that accurately reflects the actual shale internal microstructure was established. Finally, the corresponding mechanical parameters were assigned to the corresponding mineral elements. The mechanical parameters of various minerals were determined by nanoindentation experiments and from the literature data (Kumar et al., 2015; Li et al., 2019; Veytskin et al., 2017).

$$f(x,y)=\begin{bmatrix} f(1,1) & f(1,2)\cdots f(1,N) \\ f(2,1) & f(2,2)\cdots f(2,N) \\ \cdots & \\ f(M,1) & f(M,2)\cdots f(M,N) \end{bmatrix} \tag{3}$$

In addition, the results of multipoint nanoindentation of the same mineral showed that the mechanical parameters of the same phase minerals were also heterogeneous at the micro level and obeyed the Weibull distribution. The statistical distribution characteristics of the mechanical parameters were also considered in the RFPA^{3D} numerical code, which also included the Weibull distribution function (Weibull, 1951), as in Eq. (4). The specific mechanical parameter values of various minerals are shown in Table 2 (as nanoindentation experiments are not the focus of this paper, they are not described in detail here).

$$P(u)=\frac{m}{u_0}\left(\frac{u}{u_0}\right)^{m-1}\exp\left(\frac{u}{u_0}\right)^{m} \tag{4}$$

where u is an element's mechanical parameter, such as strength, Poisson's ratio, and elastic modulus; u_0 denotes a scaling parameter; and m denotes the homogeneity index, which affects the form of the distribution function. The substance becomes more homogenous as the homogeneity index increases (Tang, 1997).

The object of study in this paper is to select the region of interest from Fig. 3 with a size of 16 × 8 × 4 μm. Shale mineral particle sizes are generally between 3.2 and 35 μm (Lei et al., 2015). Considering that the calculation speed was improved without affecting the accuracy of the model when building the numerical model, the pixels of FIB-SEM images were reduced by two times, and one image was read at each interval. That is, the image spacing was 40 nm. A total of 100 FIB-SEM images were selected. Therefore, the size of the cell was 40 × 40 × 40 nm. The number of elements in the shale specimens was 8 million, and the total number of elements, including the upper and lower loading plates, was 8.8 million. According to the method described above, the three-dimensional numerical model of shale was reconstructed at the microscale, and the mechanical parameters of each mineral listed in Table 1 were assigned to the corresponding elements. Fig. 14 shows the numerical model of a shale specimen reconstructed in RFPA^{3D}, which is represented by the elastic modulus diagram; the color represents the elastic modulus of each element in the numerical model, as shown in the legend. In Model 1, as shown in Fig. 10(a), the blue minerals are pyrite, the yellow minerals are quartz-dominated carbonate matrices, and the red minerals are organic matter with contents of 24.64%, 46.13%, and 29.32%, respectively (as shown in Table 2). In Model 2, as shown in Fig. 10(b), the dark blue minerals are pyrite, the light blue minerals are calcite-dominated silicate matrix, the green minerals are quartz-dominated carbonate matrix, and the red minerals are organic matter with 9.88%, 9.94%, 69.55%, and 10.22% contents, respectively (as shown in Table 2). Uniaxial compression was performed for Model 1, and uniaxial compression and uniaxial tension numerical tests were performed for Model 2. The loading rate was 2.4e−4 μm/step for the uniaxial compression numerical test and 2.4e−5 μm/step for the uniaxial tension simulation tests.

Table 1
Material properties of the shale FE model (Kumar et al., 2015; Li et al., 2019; Veytskin et al., 2017).

	E_m, MPa	F_m, MPa	m	ν	φ, °	C/T
Organic matter	20000	60	2.5	0.34	35	10
Carbonates (calcite)	70000	190	3	0.31	35	15
Silicates (quartz)	75000	220	3.5	0.28	35	15
Pyrite	90000	310	5	0.19	35	15

Table 2
Mineral contents of the numerical models.

Mineral content, %	Pyrite	Silicate	Carbonate	Organic matter
Model 1	24.64%	–	46.13%	29.32%
Model 2	9.88%	9.94%	69.55%	10.22%

4.2. Brief description of parallel RFPA^{3D}

High-resolution simulation of rock damage processes is an important tool for revealing complex damage mechanisms in rock mechanics studies. The parallel rock failure process analysis (RFPA) simulator uses the parallel finite element solver (OpenMP technique) to solve the stiffness as well as the stress field of the representative volume element for damage evolution analysis, and it can simulate the damage process of high-resolution rock models with high efficiency (Li et al., 2017). The numerical specimens in RFPA^{3D} are considered to comprise elements with the same form and size, with no geometric precedence in any orientation (Liang et al., 2012). RFPA^{3D} has been extensively used under various stress situations to investigate the failure processes for brittle and quasi-brittle rock materials (Liang et al., 2004; Wang et al., 2016; Yu et al., 2018l).

In the RFPA^{3D} code, the element is initially linearly elastic until it approaches the damage threshold. The maximum tensile strain criterion and the Mohr–Coulomb criterion were used to develop the damage criteria. To determine whether a fracture has begun, the maximum tensile strain criterion (Eq. (5)) is often used. The second damage threshold is the Mohr–Coulomb criterion, which is described in Eq. (6). To determine whether an element is injured in tensile mode, Mohr–Coulomb criteria were employed to determine if it was destroyed in shear mode.

The maximum tensile strain criterion is as follows :

$$\varepsilon_3 \le \frac{\sigma_{t0}}{E} \tag{5}$$

The Mohr–Coulomb criterion is as follows:

$$F=\sigma_1-\sigma_3\frac{1+\sin\varphi}{1-\sin\varphi}\ge\sigma_{c0} \tag{6}$$

During the failure process, each element in the RFPA^{3D} code had an elastic–brittle constitutive law (Liang et al., 2012). Fig. 11 shows the constitutive relationship for an element under uniaxial stress.

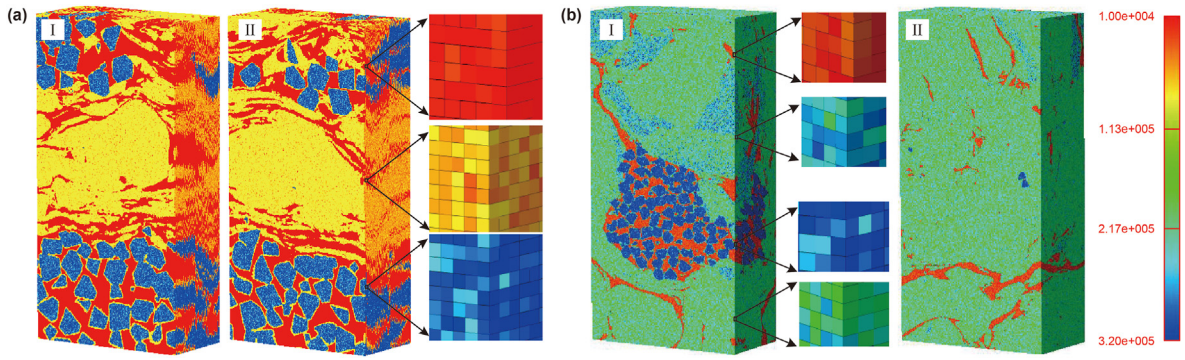

Fig. 10. Finite element numerical model, expressed by the elastic modulus; (**a**) Model 1, and (**b**) Model 2. (I) is a front view, and (II) is a back view (the colors represent the magnitude of the elastic modulus for each element in the numerical model, as shown in the legend).

Until the stress of the element meets the strength requirement, the elastic modulus remains constant at the value exhibited before loading. In elastic damage mechanics, the elastic modulus of the element may decrease progressively as damage develops until the stress reaches a level that causes the element to fail (Liang et al., 2012). The elastic modulus of the damaged element is determined as follows:

$$E = (1 - D)E_0 \tag{7}$$

where D represents damage and E and E_0 represent the elastic moduli of the damaged and undamaged materials, respectively.

The evolution of damage variable D under uniaxial tension can be expressed as follows (corresponding to the red solid line on the negative X-half-axis in Fig. 11) (Zhu and Tang, 2004):

$$D = \begin{cases} 0 & \overline{\varepsilon} > \varepsilon_{t0} \\ 1 - \dfrac{\sigma_{rt}}{\overline{\varepsilon} E_0} & \varepsilon_{tu} < \overline{\varepsilon} \le \varepsilon_{t0} \\ 1 & \overline{\varepsilon} \le \varepsilon_{tu} \end{cases} \tag{8}$$

$$\varepsilon_{tu} = \eta \varepsilon_{t0} \tag{9}$$

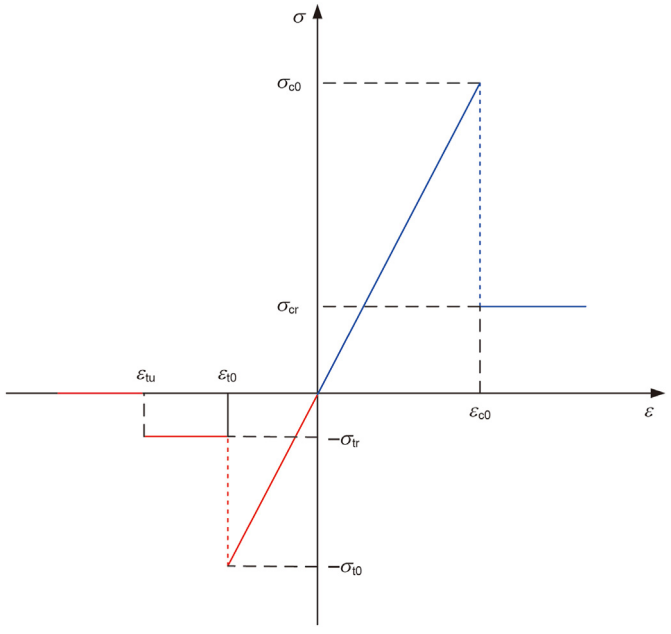

Fig. 11. Elastic-brittle damage constitutive law of elements.

where $\overline{\varepsilon}$ is the equivalent principal strain. It is expressed as follows (Zhu and Tang, 2004):

$$\overline{\varepsilon} = -\sqrt{\langle -\varepsilon_1 \rangle^2 + \langle -\varepsilon_2 \rangle^2 \langle -\varepsilon_3 \rangle^2} \tag{10}$$

where ε_1, ε_2, and ε_3 are the three principal strains, and $\langle x \rangle$ is a function defined as follows:

$$\langle x \rangle = \begin{cases} x & x \ge 0 \\ 0 & x < 0 \end{cases} \tag{11}$$

In the shear failure mode, the damage variable D may be defined as follows (corresponding to the blue solid line on the positive X-half-axis in Fig. 11):

$$D = \begin{cases} 0 & \varepsilon_1 < \varepsilon_{c0} \\ 1 - \dfrac{\sigma_{rc}}{\varepsilon_1 E_0} & \varepsilon_{c0} \le \varepsilon_1 \end{cases} \tag{12}$$

According to the aforementioned elastic damage constitutive rule, the element progressively degrades. The finite element analysis will come to a standstill if the modulus is set to zero. As a result, the limiting elastic modulus is given as 10−5.

5. Numerical simulation results and analyses

This study aimed to demonstrate how shale microstructure and stress state influence fracture characteristics and mechanical behavior in shale. Specifically, we qualitatively and quantitatively studied the propagation of microscopic cracks in different minerals under the same applied stress state of different models and the same model under different applied stress states. The significant influence of the microstructure and applied stress state on crack propagation was demonstrated.

To weaken the influence of the initial content of minerals, this paper uses the failure coefficient K to describe the failure percentage of different minerals per unit volume quantitatively. If the coefficient is smaller, then the crack is less prone to initiation and propagation. In contrast, if the coefficient is larger, then the crack is more prone to initiation and propagation. The coefficient formula is as follows:

$$K_{i,j} = \frac{V_{i,j}^D}{V_{i,j}^V} \ (i = Sh, Te, To;\ j = c, s, p, o) \tag{13}$$

where j represents the name of the mineral, c represents the carbonate matrix, s represents the silicate matrix, p represents pyrite, and o represents organic matter; i represents the mineral failure attribute, Sh represents the mineral content of shear failure, Te

represents the mineral content of tensile failure, and *To* represents the total mineral content of failure (the mineral content of shear failure plus the mineral content of tensile failure); $V^D_{i,j}$ represents the failure mineral content; and $V^V_{i,j}$ represents the mineral content.

5.1. Model 1

The crack propagation of Model 1 under uniaxial compressive stress proceeded through five stages: no increase, slow increase, rapid increase, sharp increase, and stable. Under uniaxial compressive stress, Model 1 demonstrated predominant tensile failure and less shear failure. This result is also consistent with Kranz (1979), who found that the shear strength of brittle materials is greater than the tensile strength of the material. As a result of the failure properties, when the sample finally fails, the total failure coefficients of pyrite, organic matter, and carbonate matrix follow the order below: pyrite ≈ organic matter > carbonate matrix ($K_{p,To} \approx K_{o,To} > K_{c,To}$); the tensile failure coefficients were ranked as follows: pyrite > organic matter > carbonate matrix ($K_{p,Te} > K_{o,Te} > K_{c,Te}$ and the order of the shear failure coefficients was as follows: organic matter ≫ carbonate matrix≈ pyrite ($K_{o,Sh} \gg K_{c,Sh} \approx K_{p,Sh}$). Therefore, it can be the failure of Model 1 under uniaxial compression can be inferred to be mainly caused by organic matter and pyrite. A similar conclusion was drawn by observing microfracture propagation in each mineral composition.

To observe the dynamic propagation of microcracks in different mineral compositions, Fig. 12 shows the surface crack propagation of Model 1 at points I–V at different loading stages by comparing the mineral distributions of the specimens in Fig. 10(a). Under an external load, tensile stress concentrations were initially generated in the organic matter (Fig. 12(a-I) and Fig. 12(b-I)), and a small number of acoustic emission events were generated (Fig. 12(c)). In I–II, crack initiation and propagation occurred as the tensile stress was concentrated with increasing load (Fig. 12(a-II) and Fig. 12(b-II)), and acoustic emission events increased gradually with increasing load. In addition, an obvious displacement discontinuity appeared, and it was mainly caused by the obvious differences in some mechanical parameters, such as the strengths and elastic moduli of minerals at the junction of pyrite and organic matter. A large number of acoustic emission events then resulted between occurrences III–IV. Observations of the cracks on the specimen surface indicated large amounts of crack initiation and propagation on the front side of the specimen (Fig. 12(a-III)–(a-IV)). No crack initiation was found on the back, and the cracks that initiated in the previous stage extended upward along a direction parallel to the loading (Fig. 12(b-III)–(b-IV)). In IV–V, the acoustic emission events were significantly reduced, and no cracks were initiated on either the front or back sides of the specimens (Fig. 12(a-V) and 12(b-V)). The cracks were mainly concentrated in the lower part of the specimen, where the fragmentation fracture model appeared (Fig. 12(a-V) and Fig. 12(b-V)) because a large amount of organic matter was wrapped around large grains of pyrite in the lower part of the specimen. Therefore, an inhomogeneous distribution of minerals led to an inhomogeneous distribution of cracks, and the final fracture surface of the specimen was likely to appear at the location where cracking initiated at the beginning of loading. The distribution of pyrite particles determined the crack expansion path, and complex cracks were easily formed at the aggregation of a large number of pyrite particles. As the middle part of the specimen constituted a more homogeneous carbonate matrix, the cracks in the lower part of the specimen gradually expanded toward the middle. Finally, two typical splitting cracks running approximately parallel to the loading direction were formed from the bottom to the middle of the sample (Liang et al., 2012). In addition, under the influence of the three-phase spatial distribution of minerals, the stress–strain curve of this model did not exhibit obvious brittle damage characteristics and showed high residual strength. The strength and elastic moduli were 58.75 MPa and 73,711 MPa, respectively (Fig. 12(c)).

The microscopic crack morphology of shale under loading is very complex. To study the mechanism for microscopic crack propagation, we made six slices of the specimen (i.e., slice #1, slice #2, #slice #3, slice #4, slice #5, and slice #6), which are located at distances of +XY 0, 0.8, 1.6, 2.4, 3.2, and 4.0 μm, respectively (Fig. 13(I)). Fig. 13(II–V) shows the internal crack propagation of Model 1 at different compressive stress loading stages, in which black represents the failure element. Most of the cracks initiated in the organic matter around pyrite and propagated with the organic matter around pyrite (Fig. 13(II)). As the load increased, the cracks deflected or bifurcated at the location of pyrite; occasionally, the cracks crossed the pyrite particles or ended inside the pyrite, and serious crack propagation occurred after the peak (Fig. 13(III–IV)). As the load continued to increase, especially after the peak, some of the pyrite particles were damaged (Fig. 13(IV–V)). This primarily arose because pyrite had relatively high homogeneity, large mechanical parameters, and strong integrity. Therefore, cracks could not easily form, and the accumulation of energy led to particle failure. However, whether the crack ended inside or across pyrite or pyrite particle failure occurred, these phenomena are undesirable in the fracturing of shale reservoirs because propagation of these cracks requires large amounts of energy.

The distribution of minerals plays a very important role in determining the fracture mode (Wang et al., 2015), and the failure mechanisms of different mineral components are also quite different. Fig. 14 presents the dynamic evolution characteristics for the failure percentage of each mineral in Model 1 under compressive loading. The dynamic evolution trends for the failure percentage of each mineral with increasing strain were basically the same and can be roughly divided into five stages: (A) no increase, (B) slow increase, (C) rapid increase, (D) sharp increase, and (E) stable. Fig. 14(a) shows the variations in the dynamics of the shear failure percentage for each mineral. The failure percentage was small for each mineral. In stage A, almost no mineral failure occurred. In stage B, the shear failure percentage of organic matter increased slowly, and the increased amplitude gradually increased with increasing strain; however, the shear failure percentage of the other two minerals almost did not increase. In stage C, in which the percentage increase in shear failure of the organic matter increased consistently, the other two minerals showed slow increases. In stage D a sharp increase in the percentage of organic matter shear failure and a slight increase for the remaining two minerals occurred. In stage E, the percentage of shear failure for each mineral was stabilized. In Model 1, the shear failure percentage of organic matter was the largest, and the shear failure percentage of the carbonate matrix was slightly larger than that of pyrite in stages B, C, and D. After stage D, the shear failure percentages of carbonate and pyrite were almost the same.

Fig. 14(b) shows the dynamic evolution of the tensile failure percentage for each mineral. The tensile failure percentage for each mineral was large. With increasing strain, the tensile failure percentage of the three minerals increased, but the ranges of increase were slightly different. Generally, pyrite showed the largest increase, organic matter showed the second largest increase, and the increase for the carbonate matrix was the smallest. In stage A, almost no minerals failed; in stage B, the tensile failure percentages of all three minerals increased slowly; in stage C, the tensile failure percentages of all three minerals increased greatly; and in stage D, the tensile failure percentages of all three minerals increased

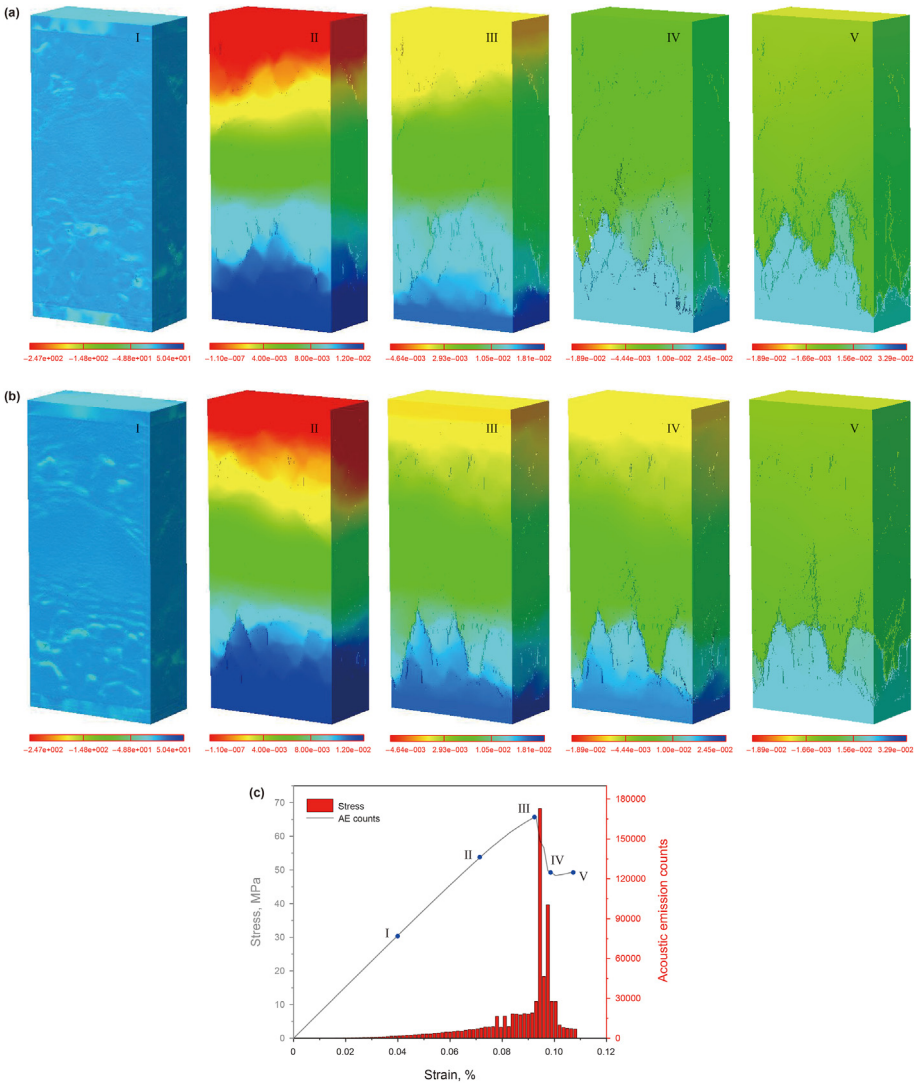

Fig. 12. Surface crack propagation of Model 1 at different compressive stress loading stages; (**a**) front view, (**b**) back view, (**c**) stress–strain curve related to AE counting. I is the minimum principal stress diagram, in MPa, and II–V are vertical displacement diagrams, in microns; (**a**) I–V and (**b**) I–V correspond to points I–V in (**c**), respectively.

sharply. In stage E, the tensile failure percentage of the carbonate matrix stabilized, while the tensile failure percentages of the remaining two minerals increased slightly. In Model 1, pyrite had the largest tensile failure percentage, followed by organic matter, and carbonate had the smallest tensile failure percentage. This result differed from our general perception, and the tensile failure percentage for pyrite was surprisingly the largest. The reason is that pyrite was located near organic matter, and most of the pyrite was wrapped by organic matter. Cracks often initiate at junctions between organic matter and pyrite, which results in stress concentrations. This leads to further crack propagation through organic matter and pyrite, but the organic matter hinders crack propagation to some extent. Therefore, a large number of cracks reach pyrite and then propagate through pyrite. This leads to a large amount of pyrite tensile damage. This phenomenon explains the unsatisfactory fracturing seen for shale reservoirs with relatively high brittleness indexes. Due to the small percentage of shear failure, the dynamic evolution characteristics for the total failure percentages of each mineral (Fig. 14(c)) are basically the same as those for the tensile failure percentages (Fig. 14(b)). However, the total failure percentage for organic matter catches up with that for pyrite in phase E due to the effect of tensile failure.

5.2. Model 2

Due to the critical role that the microstructure plays in determining shale microfracture characteristics, to study the effects of different microstructures on shale microfracture characteristics, Model 2 was subjected to uniaxial compression numerical testing under the same conditions as Model 1. Both Model 2 and Model 1 contain many aggregated pyrite particles wrapped in organic matter, which have similar mineral structures. The pyrite particles of Model 1 are concentrated in the upper and lower parts of the model. In contrast, the pyrite particles of Model 2 are mainly concentrated in the middle. Therefore, a comparative study of Model 1 and Model 2 is more suitable to investigate the influence of microstructural differences on microscopic fracture characteristics. Moreover, Model 2 was subjected to uniaxial tensile numerical tests compared with the uniaxial compression test results of Model 2. This was done to study the effect of applied stress on crack characteristics.

5.2.1. Uniaxial compression

Crack development in Model 2 under uniaxial compressive stress progressed through four stages: no increase, slow increase,

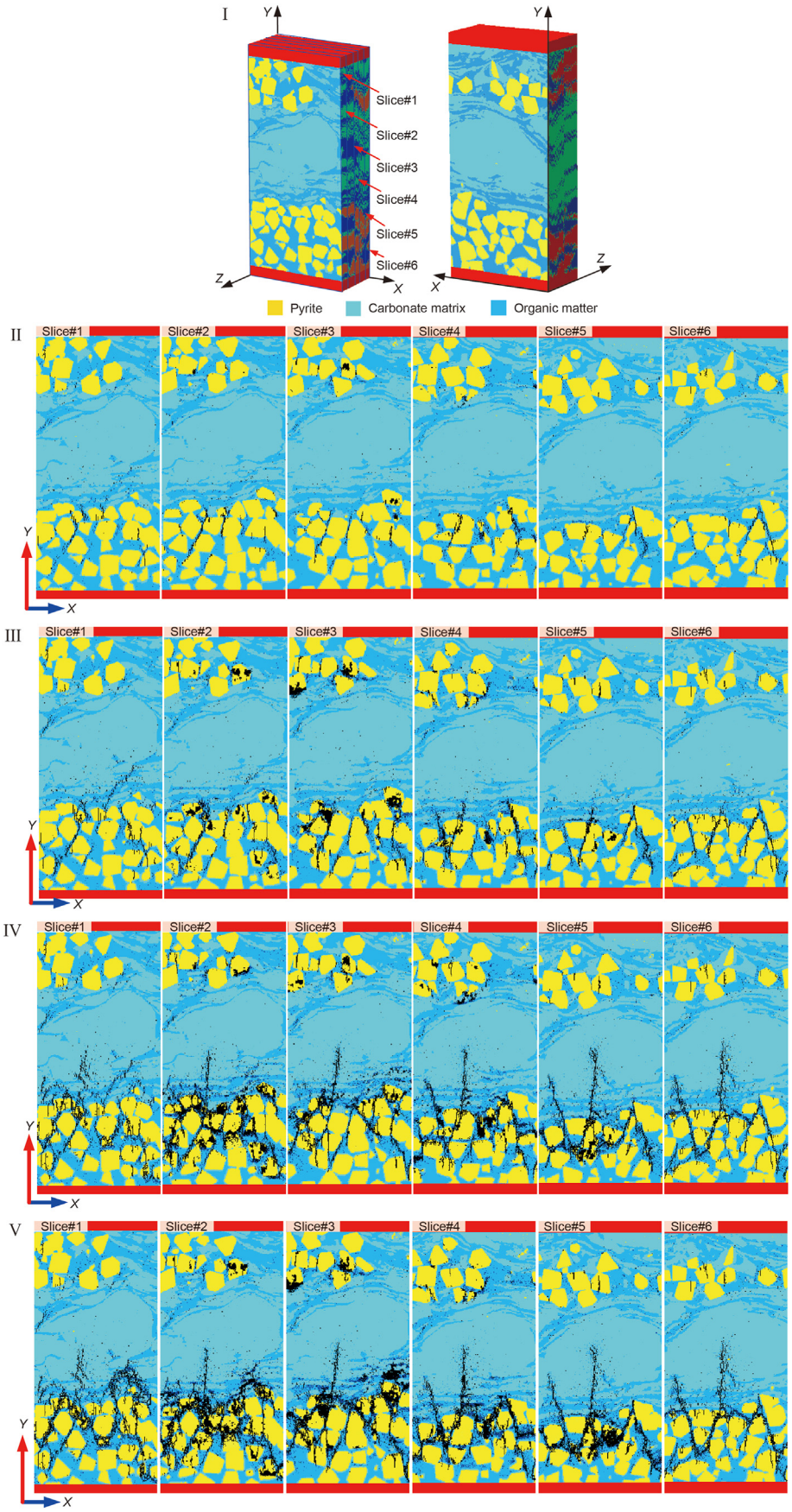
I
Y
Slice#1
Slice#2
Slice#3
Slice#4
Slice#5
Slice#6
Z
X
Pyrite
Carbonate matrix
Organic matter
II
III
IV
V

rapid increase stage, and sharp increase. Compared with Model 1, Model 2 lacks the "stable stage" in crack development, which occurred primarily due to apparent brittle failure when Model 2 failed. The mesoscopic failure mode of Model 2 under axial compressive stress was dominated by tensile failure, with less shear failure. As the sample failed, the total failure coefficients for the four minerals were as follows: pyrite > organic matter > silicate matrix > carbonate matrix ($K_{p,To} > K_{o,To} > K_{s,To} > K_{c,To}$); the sequence of tensile failure coefficients was as follows: pyrite > organic matter > silicate matrix > carbonate matrix ($K_{p,Te} > K_{o,Te} > K_{s,Te} > K_{c,Te}$); and the order of shear failure coefficients was as follows: organic matter ≫ carbonate matrix > pyrite > silicate matrix ($K_{o,Sh} \gg K_{c,Sh} > K_{p,Sh} > K_{s,Sh}$). The failure of Model 2 under uniaxial compression can be concluded to be controlled mainly through organic matter and pyrite. As the conclusions are similar to those of Model 1, the inference is that the hardest minerals (mineral particles with the largest mechanical parameters) and the softest minerals (mineral particles with the smallest mechanical parameters) tend to be decisive for failure.

To observe the dynamic propagation of microcracks in different mineral compositions, Fig. 15 shows surface crack propagation for Model 2 with different compressive stress loading stages. The mineral distribution of the specimen is compared in Fig. 10(b). Under external loading, tensile stress concentrations and a small number of acoustic emission events occurred in the organic matter (Fig. 15(a-I), Fig. 15(b-I), and Fig. 15(c)). In I–II, with increasing load, cracks initiated and propagated with the concentration of tensile stress around pyrite (Fig. 15(a-II)), and acoustic emission events gradually increased in number. In II–V, as the load continued to increase, discrete cracks continued to aggregate until a shear surface was formed (Fig. 15(a-II)–(a-V)). In front of the specimen, cracks initiated at a lower stress level (Fig. 15(a-II)). In addition, the final morphology of the crack was very complex, and many microcracks appeared around the main crack (Fig. 15(a-V))). However, on the opposite side of the specimen, crack initiation was very late, with more pronounced cracks appearing after the peak (Fig. 15(b-IV)). The final morphology of the crack was relatively simple, with an arc-shaped main crack that proceeded parallel to the loading direction. The main crack was surrounded by a few branching microcracks (Fig. 15(b-V)). The main reason for these differences between the front and back of the specimen is the heterogeneity of the spatial distributions of minerals. Under the influence of the four-phase spatial distribution of minerals, the stress–strain curve for this model exhibited more obvious brittle failure characteristics compared with Model 1 (Fig. 15(c)). The strength and elastic moduli were 65.65 MPa and 76,528 MPa, respectively.

Fig. 16 (II–V) shows the internal crack propagation processes for six slices at different strain levels. The six slices (i.e., slice #1, slice #2, slice #3, slice #4, slice #5, and slice #6) were located at distances of +XY 0, 0.8, 1.6, 2.4, 3.2, and 4.0 μm, respectively (Fig. 16(I)). Most of the cracks initiated from the organic matter around pyrite and propagated through the organic matter around pyrite (Fig. 16(II-III)). When the crack encountered organic matter during propagation, it continued to expand along the direction of the organic matter. Cracks encountering pyrite or silicate matrices are prone to offsetting and branching during propagation. The presence of hard minerals such as pyrite or silicate affected the crack propagation path and facilitated the formation of complex cracks (Fig. 16(III–V)). In addition, some of the cracks propagated across the pyrite or ended inside pyrite particles. Observation of slice #1–slice #5 showed many tiny fissures running parallel to the loading direction at aggregates of pyrite. By comparing slices #1–6, slices with high pyrite contents were found to be more prone to cracking at lower stress levels than those with low pyrite contents. The difference in mineral distribution led to obvious differences in cracks forming in different slices under the same strain. The spatial distribution of minerals and the differences in the mechanical properties of adjacent minerals greatly influenced the fracture process. This is consistent with the results of Chen et al. (2007), which indicated that the heterogeneous mineral distribution controls crack occurrence and failure in the specimens.

Fig. 17 presents the dynamic evolution of the failure percentage for each mineral in Model 2 under compressive loading. The changing trend for the failure percentage of each mineral was basically the same with increasing strain and can be roughly divided into four stages: (A) no increase, (B) slow increase, (C) rapid increase, and (D) sharp increase. Fig. 17(a) shows the dynamic evolution characteristics of the shear failure percentage for each mineral, which indicated that the shear failure percentage was generally small for each mineral. In stage A, almost no mineral failure occurred. In stage B, the shear failure percentage of organic matter increased slowly but at a progressively larger rate, but the remaining three minerals showed almost no increases. In stage C, the shear failure percentage of organic matter increased greatly, and those of the other three minerals increased slowly. In stage D, the shear failure percentage of organic matter increased sharply, and those for the remaining three minerals increased slightly. In Model 2, the shear failure percentage of organic matter was the largest, and the remaining three minerals differed very little; the failure percentage for the carbonate matrix was slightly larger, that for pyrite was the next largest, and that for the silicate matrix was the smallest.

Fig. 17(b) shows the dynamic evolution of the tensile failure percentage for each mineral, which indicated that the tensile failure percentage was large for each mineral. The tensile failure percentage of the four minerals increased with increasing strain. However, the ranges of increase were slightly different. Generally, that for pyrite was the largest, that for organic matter was the second largest, that for the silicate matrix was the second smallest and that for the carbonate matrix was the smallest. In stage A, almost no mineral failure occurred. In stage B, the tensile failure percentages of the four minerals increased slowly. In stage C, the tensile failure percentages of the four minerals increased greatly. In stage D, the tensile failure percentages of the three minerals increased sharply. In Model 1, the tensile failure percentage of pyrite was the largest, followed by those for organic matter, the silicate matrix, and carbonate. Although the pyrite particles in Model 2 were relatively aggregated, the tensile failure percentage was still larger than that for Model 1. This phenomenon further verifies the analyses of Model 1.

In addition, the dynamic evolution of the total failure percentages for each mineral (Fig. 17(b)) was in general agreement with the tensile failure percentages (Fig. 17(c)) due to the relatively small percentage of shear failure. In comparing Fig. 17(b) and Fig. 17(c), as well as Fig. 14(b) and Fig. 14(c) above, most specimen failures can be concluded to be due to tensile failure. This conclusion is consistent with the general understanding of the rock failure mechanism (Voltolini and Ajo-Franklin, 2019).

Fig. 13. Internal crack propagation for Model 1 with different compressive stress loading stages; (I) positions of the selected six sections within the numerical specimen; (II–V) internal crack evolution in specimens sliced along different Z planes. Slices were located at Z coordinates equal to 0, 0.8, 1.6, and 2.4 3.2 and 4.0 μm; II–V are at different loading stages corresponding to points II–V of the stress–strain curve in Fig. 12(c), respectively.

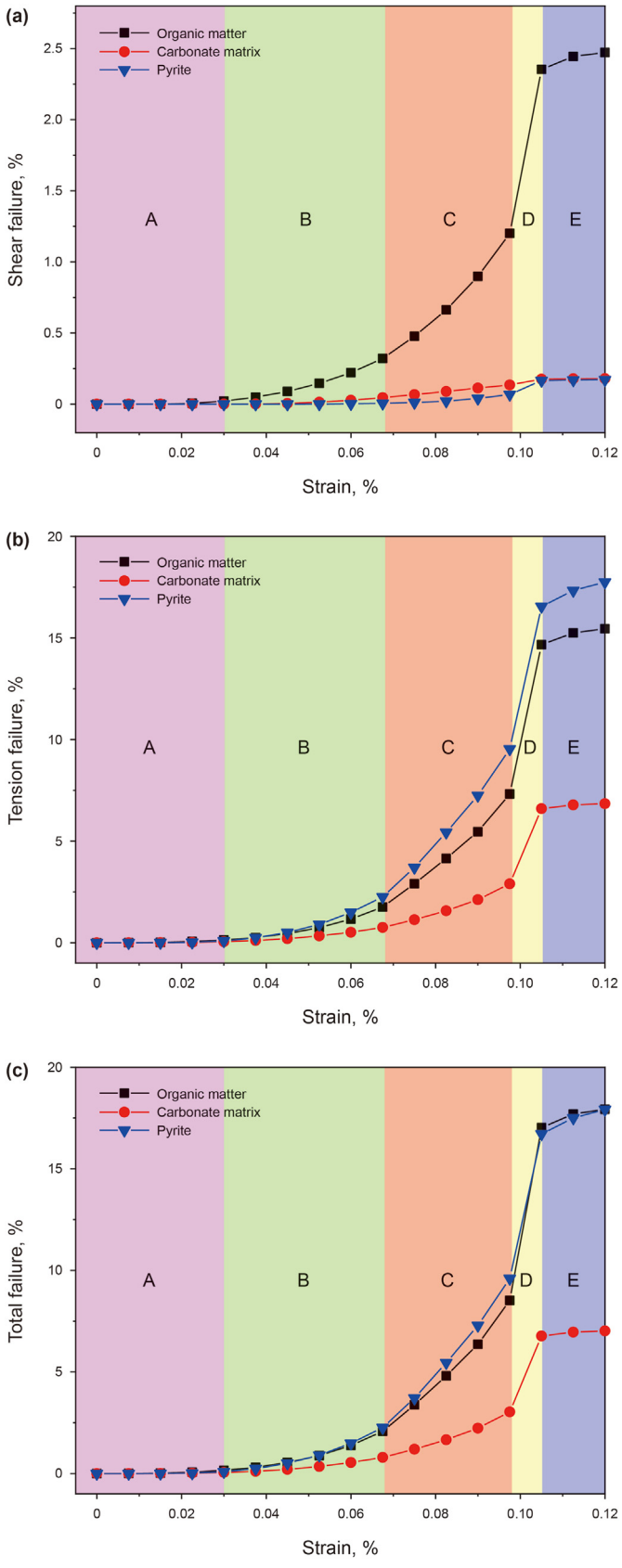

Fig. 14. Failure percentage for different mineral types in Model 1 under different strains; (**a**) shear failure percentage, (**b**) tensile failure percentage and (**c**) total failure percentage.

5.2.2. Uniaxial tension

The crack propagation of Model 1 under uniaxial tensile stress proceeded through five stages: no increase, slow increase, rapid increase, sharp increase, and stable. The failure properties of the four minerals indicate that under uniaxial tensile stress, rock fracture initiation failure was largely driven by organic matter. The order of the fracture initiation failure coefficients of the four minerals was organic matter > carbonate matrix > silicate matrix > pyrite ($K_{o,To} > K_{c,To} > K_{s,To} > K_{p,To}$). When the sample finally failed, the four minerals would fail in the following order: organic matter > pyrite > carbonate matrix > silicate matrix ($K_{o,To} > K_{p,To} > K_{c,To} > K_{s,To}$). Therefore, the failure of Model 2 under uniaxial tension can be inferred to be mainly controlled by organic matter and pyrite. The conclusion is the same as that of section 5.2.1, which indicates that the stress state does not significantly influence the order of the mineral failure coefficients.

To observe the dynamic propagation of microcracks in different mineral compositions, Fig. 18 shows surface crack propagation for Model 2 with different tensile stress loading stages. The mineral distribution of the specimen is compared in Fig. 10(b). Under external loading, tensile stress concentrations and a small number of acoustic emission events occurred in the organic matter (Fig. 18(a-I), Fig. 18 (b-I), and Fig. 18(c)). In I–II, as the load increased, cracks initiated and propagated at the location in the organic matter with a concentration of tensile stress (Fig. 18(a-II) and Fig. 18(b-II)), and acoustic emission events gradually increased in number (Fig. 18(d)). In II–V, with a continuous increase in load, the crack continued to expand along the organic lamina until it penetrated the cross-section of the specimen, forming a macroscopic fracture surface perpendicular to the loading direction (Fig. 18(a-II)–(a-V), Fig. 18(b-II)–(b-V)). During this process, acoustic emission events gradually and slowly increased in number (I–IV). However, a sudden increase in acoustic emission events occurred at point IV. In IV–V, the number of acoustic emission events remained at a high level, and macroscopic fracture surfaces were formed (Fig. 17(a-IV)–(a-V), Fig. 18(b-IV)–(b-V)). At the time of crack initiation, the rate of crack expansion and the time of formation of the final fracture surface at the front of the specimen (Fig. 18(a)) were higher than those in the back of the specimen (Fig. 18(b)). The main reason is that the aggregated pyrite on the front side of the specimen affected the stress field of the organic matter near it, resulting in earlier cracks in the front of the specimen than in the back. Fig. 18(d) shows the spatial distribution of acoustic emission (AE) events. Under tensile stress, a curved main crack surface and a branch crack finally formed along the organic laminae. In addition, a small number of acoustic emission events occurred in the middle of the specimen, where organic matter and pyrite particles were aggregated. The tensile stress–strain curve of this model was not characterized by significant brittle damage due to the influence of the four-phase spatial distribution of the minerals (Fig. 18(d)). The tensile strength was 11.32 MPa.

Fig. 19(II–V) shows the internal crack propagation process in six slices at different strain levels. The positions of the six slices (i.e., slice #1, slice #2, slice #3, slice #4, slice #5, and slice #6) were located at distances of +XY 0, 0.8, 1.6, 2.4, 3.2, and 4.0 μm, respectively (Fig. 19(I)). The crack mainly originated from the organic matter lamina at the lower part of the specimen and at the organic matter between the two pyrite particles in the middle of the specimen where pyrite aggregated (Fig. 19(II)). As the load increased, the cracks expanded gradually along with the crack initiation location, but the rate of crack expansion at the organic lamina was significantly faster than that at the pyrite aggregate (Fig. 19(II–V)). The main reason is that the tensile strength of the organic laminae was low, and the orientation of the organic laminae was approximately perpendicular to the direction of

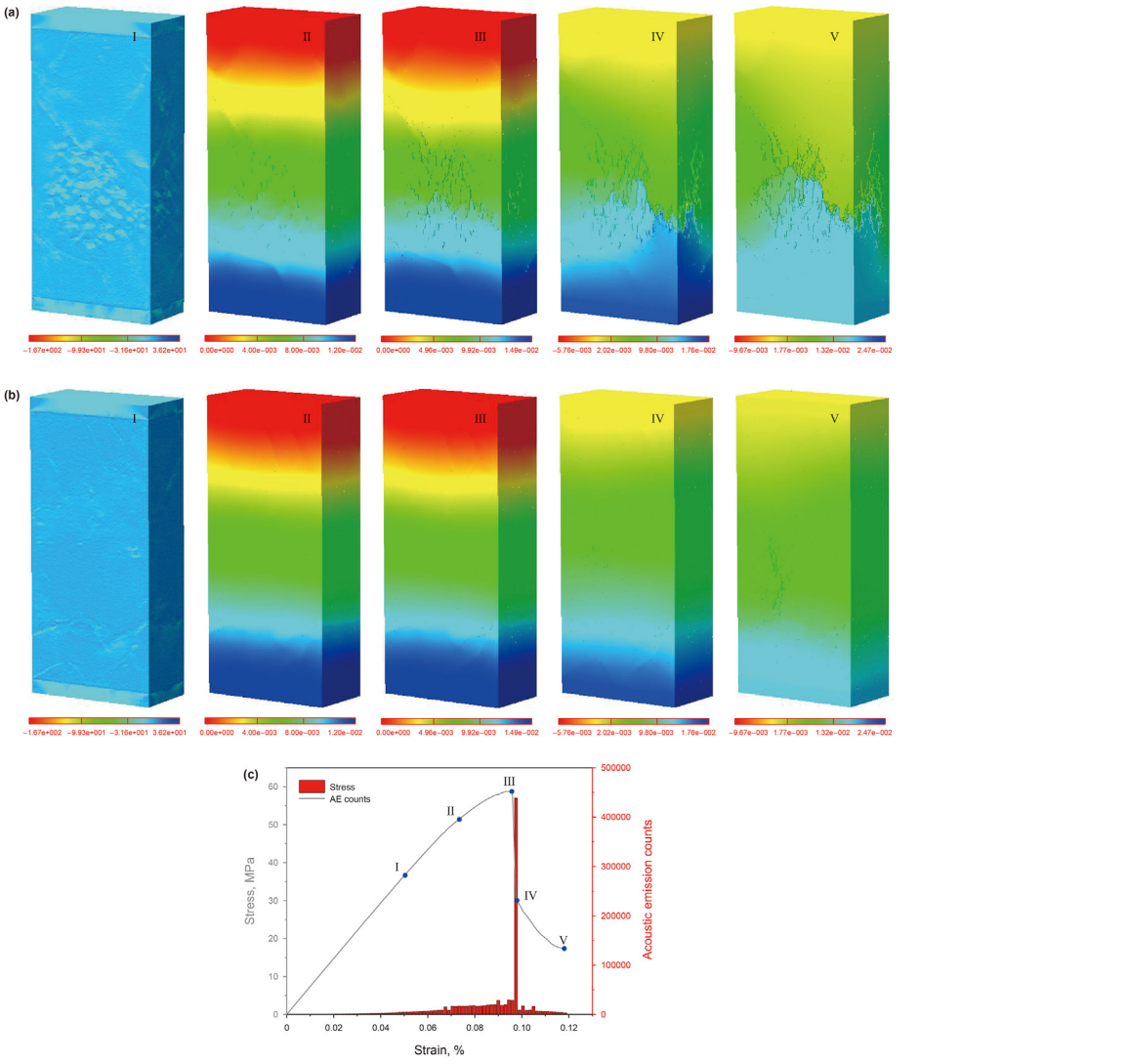

Fig. 15. Surface crack propagation for Model 2 with different compressive stress loading stages; (**a**) front view, (**b**) back view, and (**c**) stress–strain curve related to AE counting. I is the minimum principal stress diagram, in MPa, and II–V are vertical displacement diagrams, in microns. (**a**) I–V and (**b**) I–V correspond to points I–V in (**c**).

tensile stress. Therefore, the organic laminae were more likely to be destroyed under a tensile load. However, only subcracks were formed at the pyrite aggregates because the large number of pyrite particles largely prevented the cracks from extending along the organic matter between the pyrite particles. After the cracks propagated to the pyrite, most of the cracks propagated around pyrite particles, a few cracks crossed through the pyrite particles and ended inside the pyrite particles, and very few were bifurcated at the pyrite particles. Under tensile stress, the aggregation of pyrite particles easily initiated cracks but did not easily propagate cracks.

Fig. 20 shows the dynamic evolution characteristics of the failure percentage for each mineral in Model 2 under tensile loading. The trends for the failure percentages with increasing tensile strain were basically the same, and they can roughly be divided into five stages. These stages are (A) no increase, (B) slow increase, (C) rapid increase, (C) sharp increase, and (E) stable. In stage A, almost no mineral failure occurred. In stage B, the percentages of tensile failure for the four minerals increased slowly; the increase for organic matter was the largest, and the increases for the other three minerals showed little difference, although that for the carbonate matrix was largest, that for the silicate matrix was second, and that for pyrite was smallest. In stage C, the failure percentages for the four minerals increased rapidly; the increase in organic matter was still the largest, the difference in the amplitudes of the other three minerals was still minimal, and the failure percentage of pyrite exceeded that of the silicate matrix. In stage D, the failure percentages of the four minerals increased sharply, the increase in organic matter was still the largest, and the failure percentage of pyrite exceeded that of the carbonate matrix. In stage E, the failure percentages of the four minerals remained basically stable.

At the initial stage of tensile loading, organic matter failed easily, followed by the carbonate matrix and then the silicate matrix, and pyrite was the most resistant to failure. However, with increasing load, the pyrite failure percentage gradually increased, first equaling that for the silicate matrix and then that for the carbonate matrix, and the final failure percentage was ultimately second only to that for organic matter. The failure percentage for pyrite was much higher than expected. The crack initiation position was located at the organic matter lamina perpendicular to the tensile stress direction and in the same horizontal plane as the organic matter lamina wrapping the aggregation of pyrite particles. Due to the stress concentration in the organic lamina, the crack

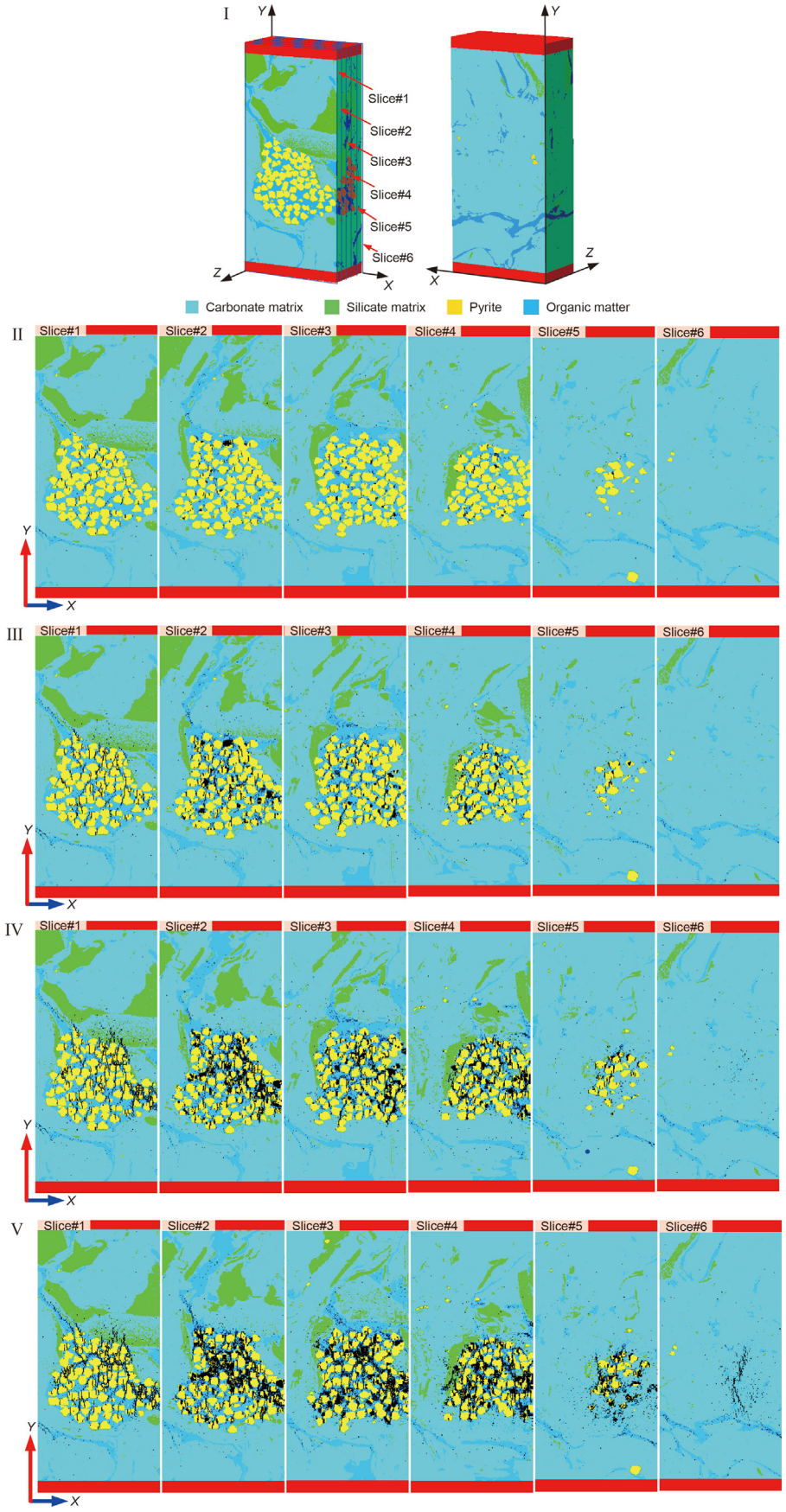

Fig. 16. Internal crack propagation for Model 2 with different compressive stress loading stages; (I) positions of the six selected sections within the numerical specimen; and (II–V) internal crack evolution in specimens sliced along different *Z* planes. Slices are located at *Z* coordinates equal to 0, 0.8, 1.6, and 2.4 3.2 and 4.0 μm, and II–V are at different loading stages corresponding to points II–V of the stress–strain curve in Fig. 15(c), respectively.

propagated along the organic lamina to pyrite. The spatial distribution of minerals, especially the differences in mechanical properties for adjacent minerals, plays important roles in the failure process.

5.3. Comparative analysis of the fractal characteristics of the 3D fracture network of numerical model 1 and numerical model 2

Fractal theory is a mathematical model used to describe an irregular object or a complicated physical process (Mandelbrot, 1983). Microstructures such as fractures in rocks have obvious fractal characteristics, and the fractal dimension can be used to properly quantify the number and complexity of fractures (Charkaluk et al., 1998; Krohn and Thompson, 1986). The box-counting fractal dimension is a representation of the fractal dimension, and its mathematical calculation is relatively simple and suitable for characterizing the spatial distributions of cracks (Ju et al., 2018). The basic principle is to cover the crack with a cubic box of side length r. The number of boxes passing through the crack is denoted as $N(r)$. The formula for the box-counting fractal dimension is as follows:

$$D_{3d} = -\lim_{r\to 0}\frac{\log N(r)}{\log r} \tag{14}$$

A series of r values and corresponding $N(r)$ values are obtained by varying the r values, i.e., the dimensions of the box, and then the logarithmic values of the two are obtained separately. Then, the obtained logarithmic values are linearly fitted using the least squares method, and the slope D_{3d} is the fractal dimension of the counting box.

Fig. 21 shows the dynamic evolution of the fractal dimension under compressive stress, which can be roughly divided into four stages, namely, A) the fast-growth stage, B) the slow growth stage, C) the "jump" growth stage, and D) the smooth stage. In stage A, the fractal dimensions of Model 1 and Model 2 increase greatly with increasing strain. The energy accumulated in the preloading stage was released faster at this stage, which promoted simultaneous initiation and expansion of multiple fractures in the rock sample and resulted in a faster increase in the fractal dimension. In stage B, the increases in the fractal dimensions of both Model 1 and Model 2 became slower because almost no crack generation occurred in this stage, and crack extension was predominant. In stage C, the fractal dimensions of Model 1 and Model 2 both showed a "jump" in growth at a strain corresponding to the peak strength. The strain corresponding to the peak strength of Model 1 was 0.096%, and the strain corresponding to the peak strength of Model 2 was 0.093%. Therefore, the "jump" growth of Model 2 occurred earlier than that of Model 1. The fractal of stage D was almost unchanged, and almost no crack initiation or expansion occurred. In the overall loading process, the increasing trends for the fractal dimensions of Model 2 and Model 1 were almost equivalent. However, the fractal dimension of Model 1 was always greater than that of Model 2. The reason is that in comparing Model 1 and Model 2, the distribution of pyrite in Model 1 was relatively scattered, the distribution of pyrite in Model 2 was relatively concentrated, cracks easily initiated at the interfaces between pyrite and other minerals, and pyrite contributed greatly to the complexity of the crack network.

6. Scanning electron microscopy analysis

Scanning electron microscopy (SEM) was utilized to study the microstructure and morphology of the samples described in section 5 under external force stimulation, and the results are shown in Fig. 22. From the backscatter images, compositional variation in

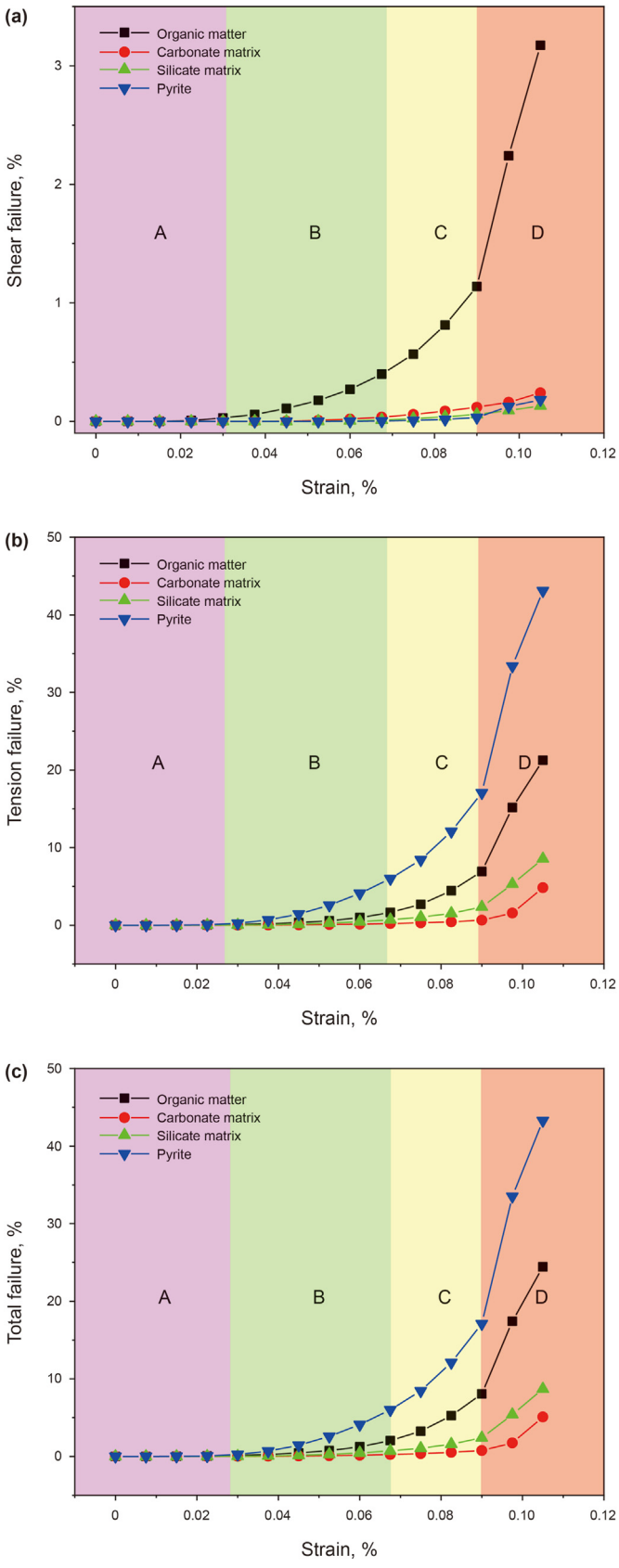

Fig. 17. Failure percentage for different mineral types in Model 1 under different strains; (**a**) shear failure percentage, (**b**) tensile failure percentage, and (**c**) total failure percentage.

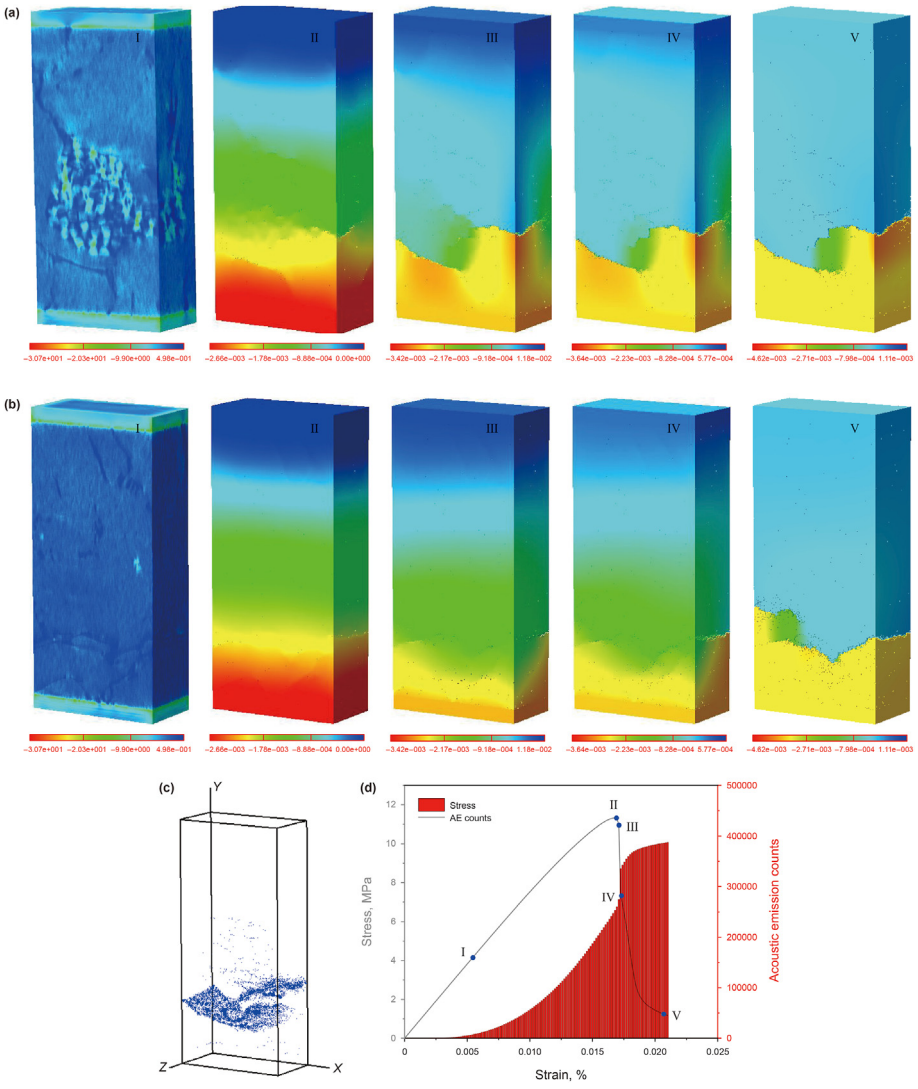

Fig. 18. Surface crack propagation of Model 2 with different tensile stress loading stages; (**a**) front view; (**b**) back view; and (**c**) spatial distribution of acoustic emission (AE) events. (**d**) Stress–strain curve related to AE counting. I is the minimum principal stress diagram, in MPa, and II–V are vertical displacement diagrams, in microns. (**a**) I–V and (**b**) I–V correspond to points I–V in (**c**).

dark and bright areas can be observed in which mineral particles such as pyrite (Py), dolomite (Dol), quartz (Qtz), calcite (Cal), clays (Cly), organic matter (Org) and micropores (inter-OMP) in minerals can be identified. When imaged in backscatter mode under SEM, pyrite appears as a bright element, whereas organic matter appears as dark masses. The SEM images on the left side of Fig. 22(a)–(e) all show the main crack, significant differences in width, tortuosity, and geometric structure. Fig. 22(a) shows how the shape of the quartz grains on the left side of the sample greatly influences the formation of the main crack. From top to bottom, the crack first spreads along the junction of quartz grains and clay minerals, bypasses the boundary of the quartz area, and then deviates into the interior of the quartz grain and penetrates through it. In Fig. 22(b) and (c), the main crack initiates and propagates along with organic matter adjacent to clay minerals, and its width is significantly smaller than in Fig. 22(a), (d), and (e). The size of the main crack shows that organic matter limits its width. The secondary fracture in Fig. 22(d) and the main fracture in Fig. 22(e) are mainly affected by calcite veins, and cracks initiate and propagate in the clay minerals adjacent to the calcite veins. Considering that all models were formed and tested under the same conditions, differences in the width, curvature, and geometry of the main crack imply that the microstructure of the rock has a significant impact on the fracture behavior, and the microstructure matters for crack propagation.

To compare the microcracking behavior of shales possessing different microstructures, particularly the propagation pattern of the crack after it meets pyrite, zoomed-in views of the spatial distribution of microcracks are shown on the right side of Fig. 22. To illustrate and describe the effect of pyrite on crack propagation, the microcracks around pyrite are represented by red lines, while C is used to express the cracks. The magnified SEM image of sample A (Fig. 22(a)) region I shows a macroscopic crack with a large opening on the right edge of pyrite particles Py1 and Py2. However, the opening of this crack decreases when passing through the pyrite particles. The pyrite particles prevent the fracture from opening. On the left side of the pyrite grains, Py1 and Py2 are two short and thin microscopic cracks, C2 and C3, which propagate around grains Py1 and Py2. In region II, crack C first passes through the pyrite particles Py1 top to bottom, causing part of the Py1 particles to break. Then, it moves around the edges of the particles. In region III, a bifurcated crack C1 forms on the left side of pyrite particle Py1 and extends

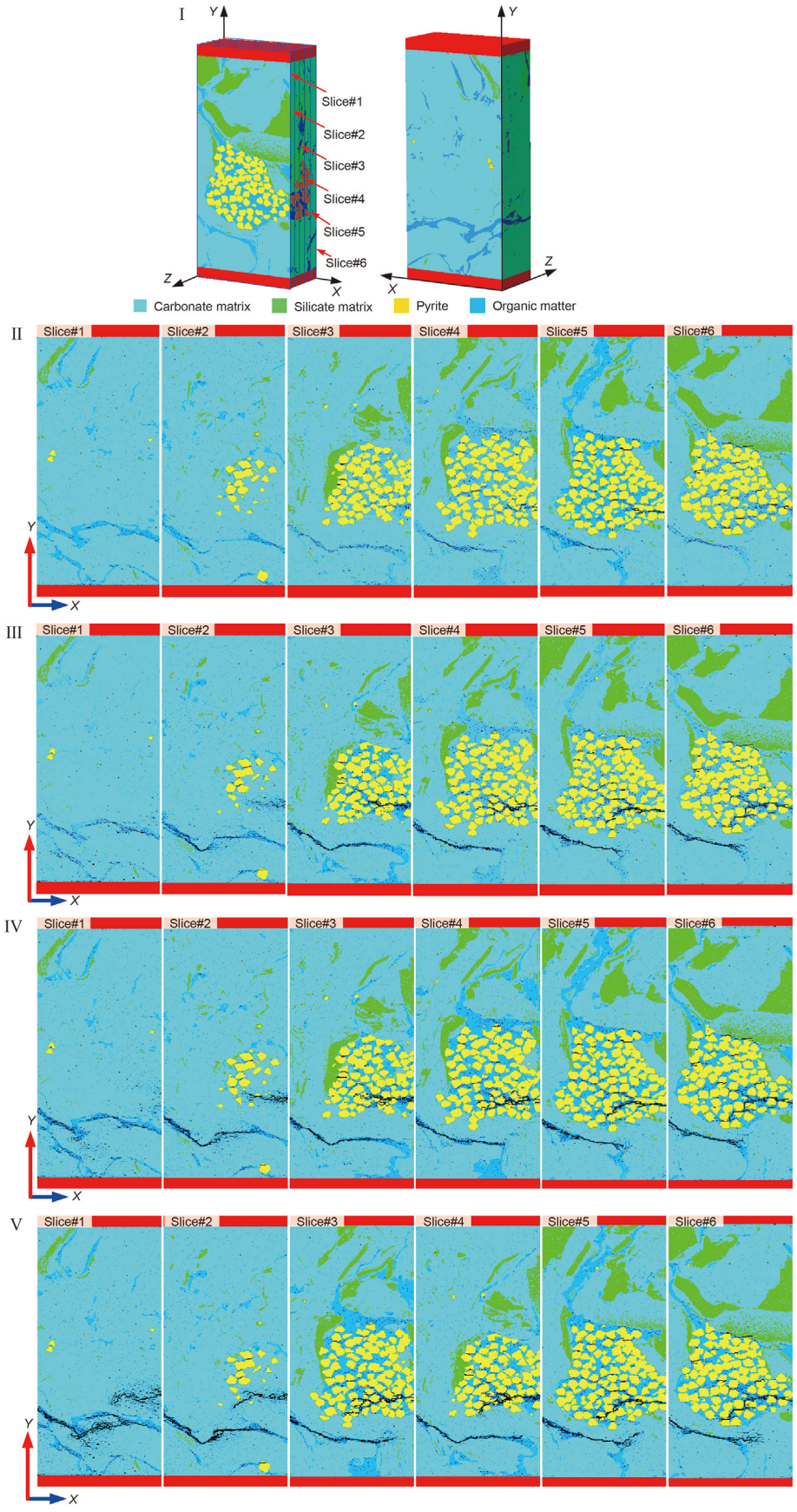
I
Y
Slice#1
Slice#2
Slice#3
Slice#4
Slice#5
Slice#6
Z
X
Carbonate matrix
Silicate matrix
Pyrite
Organic matter
II
III
IV
V

Fig. 19. Internal crack propagation for Model 2 with different tensile stress loading stages; (I) positions of the selected six sections within the numerical specimen, (II–V) internal crack evolution in specimens sliced along different *Z* planes. The slices are located at *Z* coordinates equal to 0, 0.8, 1.6, and 2.4 3.2 and 4.0 μm, and II–V are at different loading stages corresponding to points II–V of the stress–strain curve in Fig. 18(d), respectively.

into the main crack. Around the Py2 particles, however, only microscopic cracks are generated. This phenomenon occurs around Py3 and Py4 in region IV, around Py3 and Py4 in region V, and around Py1 in region VI. In region IV, crack C1 extends along the edge of Py1. After meeting Py2, it bifurcates into cracks C3 and C4. In region V, pyrite particles Py1 and Py2 are split and broken. In Region VI, pyrite particle Py4 hinders the stripping of block B from the sample, which is the key link between block B and the sample. The width of cracks generated in regions I and III > the width of the cracks generated in regions V and VI > the width of the cracks generated in regions II and IV. The cracks in region I and region III are main cracks, while those in the other regions are bifurcated cracks formed by extending the main crack to its end.

In the magnified SEM image of sample B (Fig. 22(b)) region I, crack C terminates at the edge of pyrite particle Py. In region II, crack C1 is formed on the left side of mineral particle h in organic matter, and crack C2 is formed on the right side of pyrite particle py1. The pyrite particle Py2 particles and surrounding organic matter are fragmented. The crystalline mineral inclusions in organic matter are the decisive factor affecting the formation of cracks in organic matter. In region III, crack C1 in the organic matter expands to the vicinity of the edge of pyrite particle Py. The propagation directions of crack C1 change due to the influence of the pyrite particles on the nearby stress distribution. However, it does not eventually lead to crack C1 communicating with crack C2 on the left. The expansion of cracks in organic matter is severely restricted.

The SEM local enlarged image of sample C (Fig. 22(c)) region I shows that cracks C1 and C2 formed on the upper and lower sides of pyrite particles Py in the organic matter, respectively. Two cracks are twisted, and their propagation distances are short in organic matter. Undoubtedly, pyrite particles are the leading cause of cracking in organic matter. The presence of organic matter impedes the propagation of internal cracks. In region II, crack C penetrates pyrite particle Py, resulting in pyrite breaking up. In region III, crack C1 penetrates pyrite particle Py. In addition, due to the influence of Py on the stress field at the crack tip, the propagation direction of crack C2 changes.

The magnified SEM image of sample D (Fig. 22(d)) region I and region II illustrates that the fractures at the pyrite laminae follow the direction of the laminations and detour between the grains. In region III, microcracks are generated between pyrite particles Py1 and Py2.

As seen from the magnified SEM image of sample E (Fig. 22(e)) region I, cracks C1 and C2 terminate at the edges of pyrite particle Py1. As the pyrite particles Py2 collect in region I, many fine microcracks are formed, and this phenomenon also occurs where the pyrites gather in regions II and III. In region III, when crack C expands the pyrite particle Py, it bifurcates into two cracks, C1 and C2. C1 enters and terminates within the pyrite particle Py, and C2 surrounds the pyrite particle Py propagation.

Consequently, the crack characteristics (morphology and distribution, etc.) obtained from observation in the SEM image are highly consistent with those obtained from the numerical simulation experiment. Based on the physical experiments, we found the same conclusions as the numerical studies, confirming the microstructure as the critical factor affecting fracture morphology. Although pyrite is relatively low in shale reservoirs, it has a significant impact on fracture propagation. The propagation modes resulting after the intersection of cracks and pyrite are summarized in Fig. 23. The crack will terminate, detour, and bifurcate when it encounters pyrite during propagation. Furthermore, the SEM image shows that the cracks terminate within the pyrite (such as Fig. 22(e-III)), the cracks pass through the pyrite grains (such as Fig. 22(c-III)), and the pyrite grains fragment (such as Fig. 22(c-II)). The main

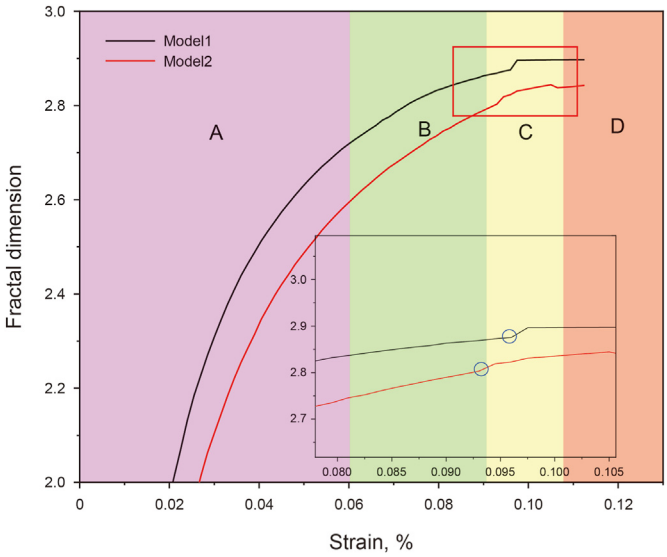

Fig. 21. Variations in fractal dimensions with strain under uniaxial compressive loading.

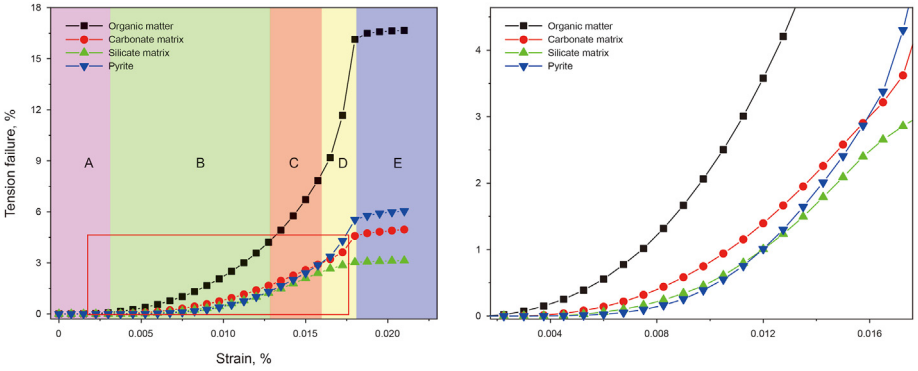

Fig. 20. Failure percentage for different mineral types in Model 1 under different strains.

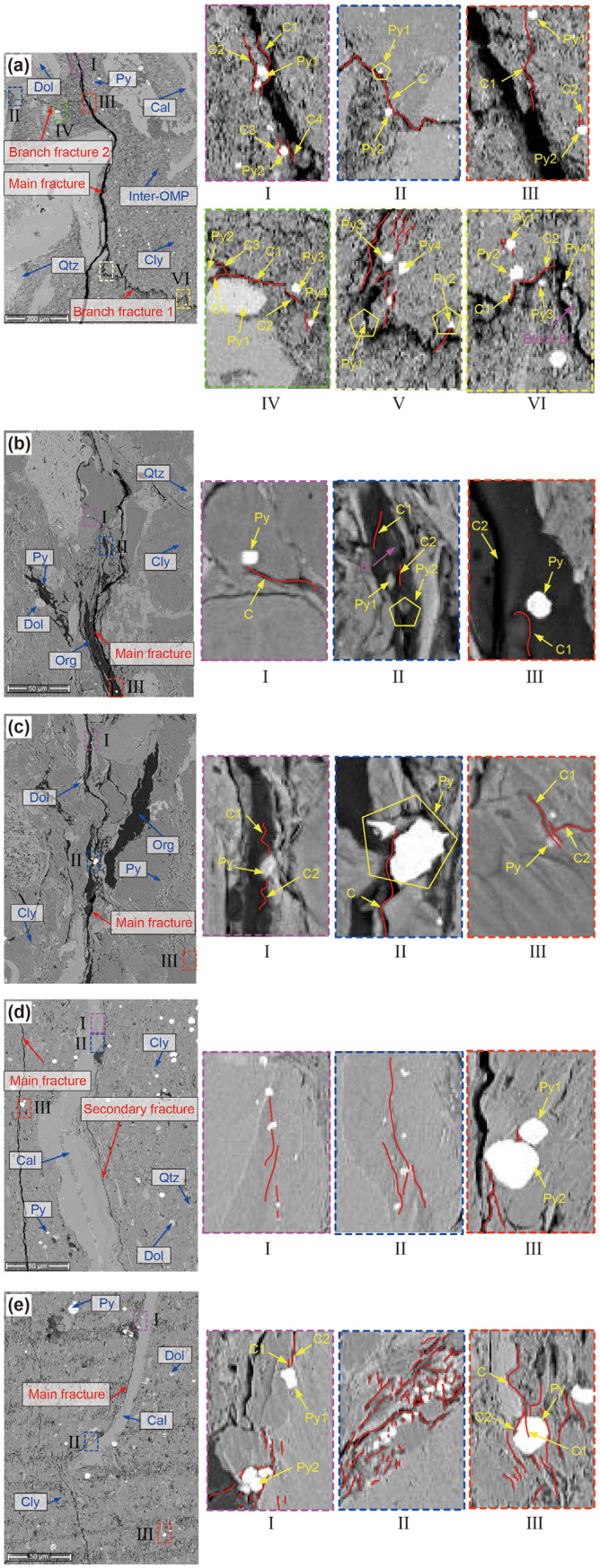

Fig. 22. Scanning electron microscope (SEM) backscattered electron diffraction (BSD) micrographs of crack propagation in shale samples stimulated by an external force. (**a**) Sample A, (**b**) sample B, (**c**) sample C, (**d**) sample D and (**e**) sample E. Heavy elements appear brighter in the backscatter mode; therefore, pyrite is seen to be predominant. Py = pyrite, Qtz = quartz, Dol = dolomite, Cal = calcite, Cly = clays, Org = organic matter and Inter-OPM = internal microscopic pore, and C = crack.

reason is that less energy is required for crack initiation and propagation at mineral grain boundaries or at preexisting microcracks, but more energy is required to split mineral grains. Conversely, when the energy applied to the sample is large, the initiation and propagation of conventional cracks cannot consume this energy, causing fragmentation of mineral grains. The experimental phenomena, which differ from our conventional understanding, further confirm the accuracy of our numerical simulation results. In addition, they verify the feasibility and efficiency of the reconstructed numerical model as a model for studying rock cracks in this study.

7. Discussion

Shale reservoirs are highly heterogeneous (Gale et al., 2014). On a macroscopic level, shale reservoirs mainly comprise different laminae, natural fractures and shale matrices (Xu et al., 2021). On a microscopic level, shales consist of many different minerals, microporosities and microcracks (Zeng et al., 2016). Based on this, scholars have performed much research to investigate the influence of macroscopic natural fractures and laminae on shale fracture extension (Jamison and Azad, 2017; Liu et al., 2018; Wang et al., 2015; Zou et al., 2016). However, few scholars have studied the influence of shale microstructural characteristics on fracture extension from a microscopic perspective. Among them, pyrite, as a brittle material, is less abundant in shale, but its influence on crack extension and brittleness cannot be ignored (Mahoney et al., 2019). Including all microstructural features in a locally tiny structure is difficult. For this reason, the purpose of the present study is to investigate the effect of pyrite on crack extension with a focus on discussion. Of course, the influence of microstructures such as micropores, fractures, and other minerals on fracture propagation characteristics is also of great significance and will be discussed in future papers.

As the mineral interface was not the focus of our research, we did not consider the mineral interface effect alone in the division of minerals. However, an obvious mineral interface was found around pyrite, especially in the transition zone between pyrite and organic matter, and the gray characteristics were similar to those of carbonate minerals. Therefore, when three categories were set during mineral classification, the interface was automatically divided into carbonate minerals. The results of the nanoscratch experiments showed that the mechanical properties of the minerals at this interface were similar to those of carbonate media, and classifying it as a carbonate matrix at the mechanical level is reasonable.

In addition, previous studies based on X-ray-CT reconstruction of 3D finite element numerical models showed that, due to the limits of CT resolution, often only larger-scale pores and fractures can be reconstructed, and identifying and reconstructing smaller-scale pores and fractures, especially the spatial distribution of multicomponent minerals, is difficult (Yu et al., 2018l; Zhao et al., 2020; Zhu et al., 2018). However, our study was based on using FIB-SEM to reconstruct the finite element numerical model, which identifies and reproduces the microstructural details inside rock, such as the spatial distributions of minerals in multiple phases (Chandra and Vishal, 2021). However, the division of minerals by the color features of FIB-SEM images is not very accurate, and errors occur. Because determination of the gray threshold is subjective, it

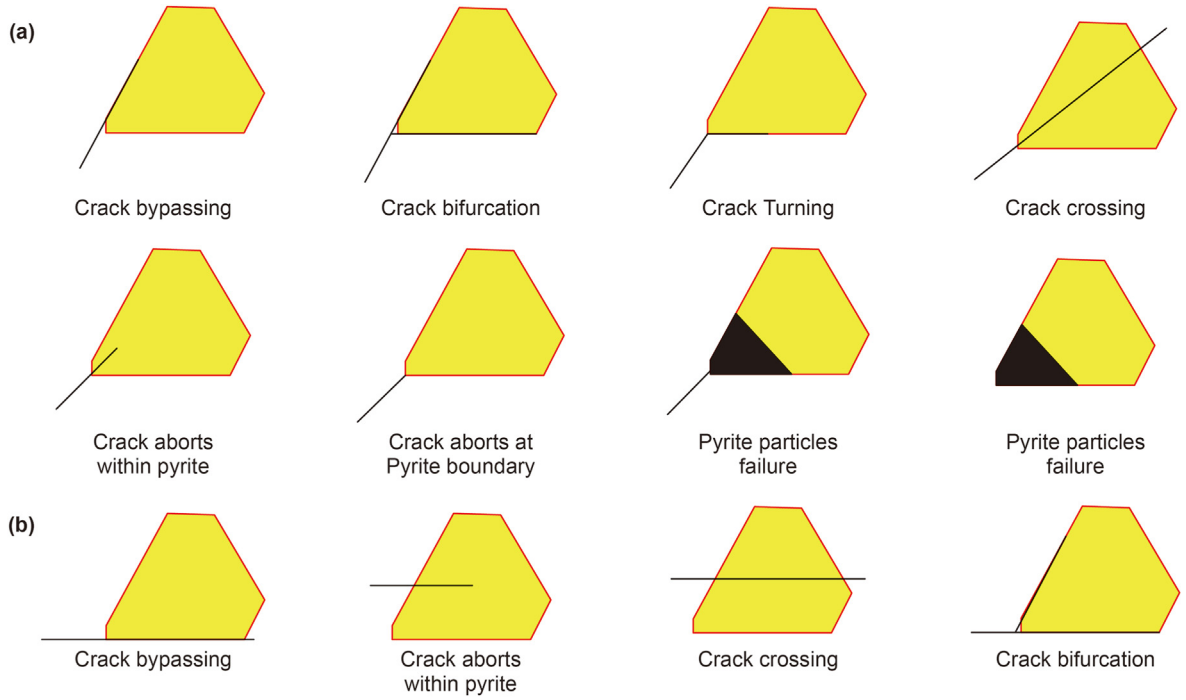

Fig. 23. Cracks intersecting pyrite under different loading modes. (**a**) Uniaxial compression test and (**b**) under uniaxial tensile test.

directly affects the results of subsequent data processing. The errors caused by this subjectivity cannot be avoided. We can only adjust the threshold of each mineral component as accurately as possible to minimize the error resulting from this subjectivity (Curtis et al., 2012). Although we used the Otsu multithreshold segmentation method to avoid human interference to the extent possible, humans still controlled class partitioning. At the same time, no definite value for the specific gray intervals corresponding to various minerals was found. Due to the principal limitations of FIB-SEM technology, when it is used to identify mineral components, they can only be roughly classified, and the method cannot identify mineral components as accurately as QEMSCAN technology. Therefore, our future research will consider the introduction of mineral identification techniques (e.g., QEMSCAN) to reconstruct a more natural and realistic numerical model for multiple mineral components and gain a deeper understanding of the mechanical behavior and damage characteristics of dense shales.

With the increasing application of high-end techniques in the structural characterization of rocks, the scope of modeling urgently needs to be extended to the mineral level. Indeed, the mineral-scale characteristics of rocks are sufficient to indicate that the study of rocks at the microscopic scale is of petrological significance (Zhang and Wong, 2018). Fracture development is deeply controlled by many geological factors, such as organic matter, brittle minerals such as pyrite, rock properties, and bedding structure. Particularly, for the “sweet spot” interval of shale (a favorable fracturing target interval), organic matter and brittle minerals provide an adequate material basis for fracture development. In brittle minerals, the mechanical parameters of pyrite particles are much larger than those of other brittle mineral components, such as carbonate and silicate. It affects the evolution and complexity of macrofractures. Therefore, pyrite should be considered and not ignored in reservoir shale fracturing. Unfortunately, due to the limitations of research methods, extensive disputes still exist about the control mechanism of rock fracture-making ability. In addition, few reports have been published on the mechanical research results of organic matter and pyrite controlling the development and evolution of fractures. Therefore, this paper selects rock samples with aggregated pyrite particles wrapped in organic matter for study. Further details clarify and reveal the relevant effects and mechanisms of organic matter and pyrite particles in the fracture-making process. This study provides a more systematic and intuitive perspective for the formation, development, and evolution of fractures in the “sweet spot” interval. It is expected to provide a reference and guidance for exploring the optimization of fracturing technology, the enhancement and improvement of oil and gas production, and other related research work in shale oil and gas exploration and development. We will select microscopic samples that have a significant impact on fractures, such as those with nanoscale pores and organic-rich laminae, to be studied in greater depth in the future.

In addition, the method proposed in this paper is mainly designed to study the mechanical properties and crack extension of shale at the microscopic scale. At present, the method has limitations for simulations of macroscale rocks. Because the numerical model based on FIB-SEM image reconstruction only covers a few microns and the sample is highly heterogeneous on the scale of a few microns, the mineral characteristics contained in the model do not directly represent shale on the macroscale. However, extending this method to macroscale studies is something we should consider in our subsequent research. The scales for scanned samples and the characterization of structural details are not consistent for any scanning technology. Therefore, the main question we should address is how to construct numerical models that do not lose structural details when used to characterize larger scales. The combination of FIB-SEM imaging with low-resolution but large-field imaging methods (e.g., X-ray microlayer imaging) may be one way to solve these problems, and it will be considered in future studies (Gerke et al., 2021). A rigorous model for characterizing the true structures of rocks is absolutely necessary for simulating both microscopic and macroscopic damage processes in rocks.

8. Conclusions

In this paper, FIB-SEM was used to capture the real microstructures of shale samples. Based on analyses of FIB-SEM image features, an improved multithreshold segmentation method was proposed for identifying and characterizing the microstructures of shale and effectively distinguishing the mineral components of shale. The processed digital images were combined with the RFPA^{3D} parallel computing numerical code to build a 3D finite element numerical model indicating the real microstructure of the shale. Thus, numerical tests of uniaxial compression and uniaxial tension were conducted on shale to study its mechanical properties and crack extension characteristics from a microscopic perspective. Moreover, the crack characteristics (shape and distribution, etc.) obtained in the numerical simulation experiment were compared with those obtained from the SEM image from the physical experiment. They were found to be highly consistent. Thus, the accuracy of the numerical simulation results further validates the feasibility and effectiveness of the numerical model reconstructed in this paper for studying rock cracks. This study provides a new tool for in-depth studies of the mechanism of shale fracturing. The conclusions are summarized as follows:

(1) Cracks tend to form at the junction of soft and hard minerals (that is, the junction of minerals that have genuinely different mechanical properties), propagate in the softer minerals adjacent to the harder minerals, and then spread along the edges of the harder minerals. Cracks are most likely to develop at the junction of soft minerals, such as organic matter, with various minerals. Hard mineral inclusions in organic matter play a decisive role in forming cracks in organic matter. Nevertheless, organic material itself hinders the expansion of its internal cracks, limiting the length and width of the cracks and causing them to become more tortuous.

(2) Under compressive loading, pyrite particles easily initiate and propagate cracks, and a more complex crack network is formed around them. Under tensile loading, aggregated pyrite particles easily initiate cracks but hinder crack propagation. Most of the crack propagation in pyrite particles is bifurcated under compressive loading, while most of the crack propagation bypasses pyrite particles under tensile loading. Even though the content of pyrite is relatively low in shale reservoirs, it has a significant impact on fracture propagation. The crack terminates, detours, and bifurcates when it encounters pyrite during propagation. Moreover, unusual phenomena such as cracks that extend into the inner part of the pyrite grains occur. These cracks end at or through the pyrite grains and split and break the pyrite grains. The main reason is that less energy is required for crack initiation and propagation at mineral grain boundaries or at preexisting microcracks, while more energy is required to split mineral grains. Conversely, when the energy applied to the sample is large, the initiation and propagation of conventional cracks cannot consume this energy, causing fragmentation of mineral grains.

(3) In the pyrite lamina, microcracks will often develop along the direction of the pyrite lamina and detour between particles of the pyrite lamina. In pyrite accumulations, dense and short microcracks can easily develop. Because the formation of these dense fractures requires much energy, it will hinder the formation of macrocracks. For dispersed and aggregated distributions of pyrite particles, the fractal dimension of cracks formed by the dispersed distribution is larger, and the crack complexity is higher. The existence of pyrite is conducive to the formation of microcracks but not conducive to the formation of macrocracks, and it hinders the opening of cracks.

(4) The tensile failure percentage for each mineral accounts for the majority of failure events. Under compressive loading, the largest tensile failure percentage was observed for pyrite, and it was influenced by adjacent organic matter. The tensile failure percentage of pyrite under tensile loading was second only to that of organic matter. Differences in mineral properties for adjacent minerals play a very important role in the failure process.

The spatial distribution of minerals affects the mechanical behavior, crack initiation location, crack propagation path, and final failure mode of shale. Stress concentration occurs easily at the junctions of different minerals or organic matter wrapped in hard minerals and results in crack initiation. Crack propagation is easily offset and branches when encountering hard minerals such as pyrite. Intricate crack networks tend to form at harder mineral inclusions, such as pyrite. Although hard minerals such as pyrite are not highly abundant in shale oil and gas reservoirs, their influence on fracturing cannot be ignored. Therefore, the influence of pyrite should not be neglected in the design and modification of fracturing.

Acknowledgements

The research work is supported by the Central Program of Basic Science of the National Natural Science Foundation of China (No. 72088101) “The theory and application of resource and environment management in the digital economy era”. The National Natural Science Foundation of China (No. 41941018). Scientific research and technological development program of RIPED, “major research of basic geologic and synergy research of engineering practice on Gulong shale oil” (No. 2021ycq01).

List of Symbols

ν	Poisson ratio
D	Damage variable
σ	Stress tensor, MPa
E	Elastic modulus of the damaged elements, MPa
σ_1	Maximum principal stress, MPa
E_m	Elastic modulus, MPa
σ_3	Minimum principal stress, MPa
E_0	Elastic modulus of the undamaged elements, MPa
σ_{c0}	Uniaxial compressive strength, MPa
F_m	Axial compressive strength, MPa
σ_{rt}	Residual tensile stress, MPa
C/T	Ratio of tensile to compressive strength
σ_{rc}	Residual compressive stress, MPa
$P(u)$	Distribution density, MPa^{-1}
σ_{t0}	Uniaxial tensile strength, MPa
m	Homogeneity index
φ	Friction angle
u	Material parameters of the element (such as Young's modulus and strength) obtained from experiments
$f(x,y)$	Initial gray value of the pixel (x,y)
u_0	The mean value of elements put into the numerical simulation program
T	Segmentation threshold
ε	Strain tensor
h	Height h of the image, pixels
$\bar{\varepsilon}$	Equivalent principal strain
μ	Mean of each category gray level

ε_1	Maximum principal strain
P	Probabilities of each category gray level
ε_2	Middle principal strain
$K_{i,j}$	Failure coefficient
ε_3	Minimum principal strain
$V_{i,j}^D$	Failure mineral content, %
ε_{c0}	Critical strain under peak compressive
$V_{i,j}^V$	Mineral content, %
ε_{t0}	Threshold strain
r	Cubic box of side length
ε_{tu}	Ultimate tensile strain
$N(r)$	Number of boxes passing through the crack
η	Ultimate tensile stress factor
D_{3d}	Fractal dimension of the counting box

References

Akono, A.T., Kabir, P., 2016. Microscopic fracture characterization of gas shale via scratch testing. Mech. Res. Commun. 78, 86–92. https://doi.org/10.1016/j.mechrescom.2015.12.003.

Bennett, K.C., Berla, L.A., Nix, W.D., Borja, R.I., 2015. Instrumented nanoindentation and 3D mechanistic modeling of a shale at multiple scales. Acta Geotechnica 10 (1), 1–14. https://doi.org/10.1007/s11440-014-0363-7.

Blair, S.C., Cook, B.G.W., 1998. Analysis of compressive fracture in rock using statistical techniques: Part II. Effect of microscale heterogeneity on macroscopic deformation. Int. J. Rock Mech. Min. Sci. 35 (7), 849–961. https://doi.org/10.1016/S0148-9062(98)00009-6.

Chandra, D., Vishal, V., 2021. A critical review on pore to continuum scale imaging techniques for enhanced shale gas recovery. Earth Sci. Rev. 217, 103638. https://doi.org/10.1016/j.earscirev.2021.103638.

Charkaluk, E., Bigerelle, M., Iost, A., 1998. Fractals and fracture. Eng. Fract. Mech. 61 (1), 119–139. https://doi.org/10.1016/S0013-7944(98)00035-6.

Chen, S., Yue, Z.Q., Tham, L.G., 2007. Digital image based approach for three-dimensional mechanical analysis of heterogeneous rocks. Rock Mech. Rock Eng. 40 (2), 145. https://doi.org/10.1007/s00603-006-0105-8.

Curtis, M.E., Sondergeld, C.H., Ambrose, R.J., Rai, C.S., 2012. Microstructural investigation of gas shales in two and three dimensions using nanometer-scale resolution imaging. AAPG (Am. Assoc. Pet. Geol.) Bull. 96 (4), 665–677. https://doi.org/10.1306/08151110188.

Gale, J.F.W., Laubach, S.E., Olson, J.E., Eichhuble, P., Fall, A., 2014. Natural Fractures in shale: a review and new observations. AAPG (Am. Assoc. Pet. Geol.) Bull. 98 (11), 2165–2216. https://doi.org/10.1306/08121413151.

Gerke, K.M., Korostilev, E.V., Romanenko, K.A., Karsanina, M.V., 2021. Going sub-micron in the precise analysis of soil structure: a FIB-SEM imaging study at nanoscale. Geoderma 383. https://doi.org/10.1016/j.geoderma.2020.114739.

Goral, J., Deo, M., McLennan, J., Huang, H., Mattson, E., 2020. Macro- and micro-compression testing of shales. J. Petrol. Sci. Eng. 2020 (191), 107034 https://doi.org/10.1016/j.petrol.2020.107034.

Gu, X., Cole, D.R., Rother, G., et al., 2015. Pores in marcellus shale: a neutron scattering and FIB-SEM study. Energy & Fuels 29, 1295–1308. https://doi.org/10.1021/acs.energyfuels.5b00033.

He, J.C., Zhang, K.S., Liu, H.B., Tang, M.R., Zheng, X.L., Zhang, G.Q., 2022. Laboratory investigation on hydraulic fracture propagation in sandstone-mudstone-shale layers. Petrol. Sci. 19 (4), 1664–1673. https://doi.org/10.1016/j.petsci.2022.03.018.

Hu, S., Liu, W.N., Liu, Y.M., Liu, K., 2022. Acoustic logging response law in shales based on petrophysical model. Petrol. Sci. 19 (5), 2120–2130. https://doi.org/10.1016/j.petsci.2022.03.015.

Jamison, W., Azad, A., 2017. The hydraulic fracture - natural fracture network configuration in shale reservoirs: geological limiting factors. J. Petrol. Sci. Eng. 159, 205–229. https://doi.org/10.1016/j.petrol.2017.09.017.

Ju, Y., Xi, C., Zhang, Y., Mao, L., Gao, F., Xie, H., 2018. Laboratory *in situ* CT observation of the evolution of 3D fracture networks in coal subjected to confining pressures and axial compressive loads: a novel approach. Rock Mech. Rock Eng. 51, 3361–3375. https://doi.org/10.1007/s00603-018-1459-4.

Kranz, R.L., 1979. Crack-crack and crack-pore interactions in stressed granite. Int. J. Rock Mech. Min. Sci. 16 (1), 37–47. https://doi.org/10.1016/0148-9062(79)90773-3.

Krohn, C., Thompson, A., 1986. Fractal sandstone pores: automated measurements using scanning-electron-microscope images. Phys. Rev. B 33 (9), 6366–6374. https://doi.org/10.1103/PhysRevB.33.6366.

Kumar, V., Sondergeld, C.H., Rai, C.S., 2012. Nano to macro mechanical characterization of shale. Nano Macro Mech. Charac. Shale. ISBN : 9781613992135.

Kumar, V., Sondergeld, C., Rai, C.S., 2015. Effect of mineralogy and organic matter on mechanical properties of shale. Interpretation 3 (3), SV9–SV15. https://doi.org/10.1190/INT-2014-0238.1.

Labani, M.M., Rezaee, R., 2015. The importance of geochemical parameters and shale composition on rock mechanical properties of gas shale reservoirs: a case study from the Kockatea shale and Carynginia formation from the Perth basin, Western Australia. Rock Mech. Rock Eng. 48 (3), 1249–1257. https://doi.org/10.1007/s00603-014-0617-6.

Lan, H., Martin, C.D., Hu, B., 2010. Effect of heterogeneity of brittle rock on micromechanical extensile behavior during compression loading. J. Geophys. Res. 115 (B1), B01202. https://doi.org/10.1029/2009jb006496.

Lei, Y., Luo, X., Wang, X., Zhang, L., Zhang, L., 2015. Characteristics of silty laminae in Zhangjiatan Shale of southeastern Ordos Basin, China: implications for shale gas formation. AAPG (Am. Assoc. Pet. Geol.) Bull. 99 (4), 661–687. https://doi.org/10.1306/09301414059.

Li, G., Tang, C.-A., Liang, Z.-Z., 2017. Development of a parallel FE simulator for modeling the whole trans-scale failure process of rock from meso- to engineering-scale. Comput. Geosci. 98, 73–86. https://doi.org/10.1016/j.cageo.2016.08.014.

Li, C., Ostadhassan, M., Kong, L., Bubach, B., 2019. Multi-scale assessment of mechanical properties of organic-rich shales: a coupled nanoindentation, deconvolution analysis, and homogenization method. J. Petrol. Sci. Eng. 174, 80–91. https://doi.org/10.1016/j.petrol.2018.10.106.

Li, Z., Wang, S., Li, L., Zhang, J., Li, T., 2021. Numerical simulation of brittleness effect on propagation behavior of glutenite hydraulic fractures. Ain Shams Eng. J. 12 (4), 3419–3427. https://doi.org/10.1016/j.asej.2021.03.015.

Liang, Z.Z., Tang, C.A., Li, H.X., Zhang, Y.B., 2004. Numerical simulation of the 3-D failure process in heterogeneous rocks. Int. J. Rock Mech. Min. Sci. 41 (3). https://doi.org/10.1016/j.ijrmms.2004.03.061.

Liang, Z.Z., Xing, H., Wang, S.Y., Williams, D.J., Tang, C.A., 2012. A three-dimensional numerical investigation of the fracture of rock specimens containing a pre-existing surface flaw. Comput. Geotech. 45, 19–33. https://doi.org/10.1016/j.compgeo.2012.04.011.

Liu, Q., Jiang, Y., Wu, Z., He, J., 2018. A Voronoi element based-numerical manifold method (VE-NMM) for investigating micro/macro-mechanical properties of intact rocks. Eng. Fract. Mech. 199, 71–85. https://doi.org/10.1016/j.engfracmech.2018.05.010.

Ma, C., Dong, C., Lin, C., Elsworth, D., Liu, X., 2019. Influencing factors and fracability of lacustrine shale oil reservoirs. Mar. Petrol. Geol. 110, 463–471. https://doi.org/10.1016/j.marpetgeo.2019.07.002.

Mahoney, C., März, C., Buckman, J., Wagner, T., Blanco-Velandia, V.-O., 2019. Pyrite oxidation in shales: implications for palaeo-redox proxies based on geochemical and SEM-EDX evidence. Sediment. Geol. 389, 186–199. https://doi.org/10.1016/j.sedgeo.2019.06.006.

Mandelbrot, B.B., 1983. The fractal geometry of nature. Am. J. Phys. 51 (3), 286–287. https://doi.org/10.1119/1.13295.

Ouchi, H., Agrawal, S., Foster, J.T., Sharma, M.M., 2017. Effect of small scale heterogeneity on the growth of hydraulic fractures. SPE Hydraulic Fracturing Technology Conference and Exhibition. https://doi.org/10.2118/184873-MS.

Ren, J., Ge, X., 2004. Computerized tomography examination of damage tests on rocks under triaxial compression. Rock Mech. Rock Eng. 37 (1), 83–93. https://doi.org/10.1007/s00603-003-0007-y.

Ren, Y., Chua, C.-S., Ho, Y.-K., 2003. Motion detection with nonstationary background. Mach. Vis. Appl. 13 (5–6), 332–343. https://doi.org/10.1109/ICIAP.2001.956988.

Rickman, R., Mullen, M., Petre, E., Grieser, B., Kundert, D., 2008. A practical use of shale Petrophysics for stimulation design optimization: all shale plays are not Clones of the barnett shale. In: SPE Annual Technical Conference & Exhibition. Society of Petroleum Engineers. https://doi.org/10.2118/115258-MS.

Sone, H., Zoback, M.D., 2013. Mechanical properties of shale-gas reservoir rocks - Part 1: static and dynamic elastic properties and anisotropy. Geophysics 78 (5), D381–D392. https://doi.org/10.1190/geo2013-0050.1.

Tang, C., 1997. Numerical simulation of progressive rock failure and associated seismicity. Int. J. Rock Mech. Min. Sci. 34 (2), 249–261. https://doi.org/10.1016/S0148-9062(96)00039-3.

Tang, J., Wu, K., 2018. A 3-D model for simulation of weak interface slippage for fracture height containment in shale reservoirs. Int. J. Solid Struct. 144–145, 248–264. https://doi.org/10.1016/j.ijsolstr.2018.05.007.

Tang, C., Tham, L., Lee, P., Tsui, Y., Liu, H., 2000a. Numerical studies of the influence of microstructure on rock failure in uniaxial compression - Part II: Constraint, slenderness and size effect. Int. J. Rock Mech. Min. Sci. 37 (4), 571–583. https://doi.org/10.1016/S1365-1609(99)00122-7.

Tang, C.A., Liu, H., Lee, P., Tsui, Y., Tham, L.G., 2000b. Numerical studies of the influence of microstructure on rock failure in uniaxial compression- Part I: Effect of heterogeneity. Int. J. Rock Mech. Min. Sci 37 (4), 555–569. https://doi.org/10.1016/S1365-1609(99)00122-7.

Tang, X., Jiang, Z., Jiang, S., Li, Z., 2016. Heterogeneous nanoporosity of the Silurian Longmaxi Formation shale gas reservoir in the Sichuan Basin using the QEMSCAN, FIB-SEM, and nano-CT methods. Mar. Petrol. Geol. 78, 99–109. https://doi.org/10.1016/j.marpetgeo.2016.09.010.

Tang, J., Wu, K., Li, Y., Hu, X., Liu, Q., Christine, E.E., 2018. Numerical investigation of the interactions between hydraulic fracture and bedding planes with non-orthogonal approach angle. Eng. Fract. Mech. 200, 1–16. https://doi.org/10.1016/j.engfracmech.2018.07.010.

Tang, J., Ehlig-Economides, C., Fan, B., Cai, B., Mao, W., 2019a. A microseismic-based fracture properties characterization and visualization model for the selection of infill wells in shale reservoirs. J. Nat. Gas Sci. Eng. 67, 147–159. https://doi.org/10.1016/j.jngse.2019.04.014.

Tang, J., Li, J., Tang, M., Du, X., Xiao, L., 2019b. Investigation of multiple hydraulic fractures evolution and well performance in lacustrine shale oil reservoirs considering stress heterogeneity. Eng. Fract. Mech. 218, 106569. https://doi.org/10.1016/j.engfracmech.2019.106569.

Tang, J., Fan, B., Xiao, L., Tian, S., Zhang, F., Zhang, L., Weitz, D., 2021. A new ensemble machine learning framework for searching sweet spots in shale reservoirs. SPE J. 26, 482–497. https://doi.org/10.2118/204224-PA, 01.
Tsafnat, N., Amanat, N., Jones, A.S., 2011. Analysis of coke under compressive loading: a combined approach using micro-computed tomography, finite element analysis, and empirical models of porous structures. Fuel 90 (1), 384–388. https://doi.org/10.1016/j.fuel.2010.08.026.
Veytskin, Y.B., Tammina, V.K., Bobko, C.P., et al., 2017. Micromechanical characterization of shales through nanoindentation and energy dispersive x-ray spectrometry. Geomechan. Energy Environ. 9, 21–35. https://doi.org/10.1016/j.gete.2016.10.004.
Voltolini, M., Ajo-Franklin, J., 2019. Evolution of propped fractures in shales: the microscale controlling factors as revealed by in situ X-Ray microtomography. J. Petrol. Sci. Eng. 188 (3), 106861. https://doi.org/10.1016/j.petrol.2019.106861.
Wang, Y., Li, X., Zhou, R., Zheng, B., Zhang, B., Wu, Y., 2015. Numerical evaluation of the effect of fracture network connectivity in naturally fractured shale based on FSD model. Sci. China Earth Sci. 59 (3), 626–639. https://doi.org/10.1007/s11430-015-5164-9.
Wang, S.Y., Sloan, S.W., Sheng, D.C., Tang, C.A., 2016. 3D numerical analysis of crack propagation of heterogeneous notched rock under uniaxial tension. Tectonophysics 677–678, 45–67. https://doi.org/10.1016/j.tecto.2016.03.042.
Wang, M., Li, M., Li, J.B., Xu, L., Zhang, J.X., 2022. The key parameter of shale oil resource evaluation: oil content. Petrol. Sci. 19 (4), 1443–1459. https://doi.org/10.1016/j.petsci.2022.03.006.
Weibull, W., 1951. A statistical distribution function of wide applicability. J. Appl. Mech. 18, 293–297. https://doi.org/10.1093/qjmam/6.4.453.
Wu, Z., Ji, X., Liu, Q., Fan, L., 2020. Study of microstructure effect on the nonlinear mechanical behavior and failure process of rock using an image-based-FDEM model. Comput. Geotech. 121, 103480. https://doi.org/10.1016/j.compgeo.2020.103480.
Xu, X., Zeng, L., Tian, H., Ling, K., Che, S., Yu, X., Dong, S., 2021. Controlling factors of lamellation fractures in marine shales: a case study of the Fuling Area in Eastern Sichuan Basin, China. J. Petrol. Sci. Eng. 207, 109091. https://doi.org/10.1016/j.petrol.2021.109091.
Yasin, Q., Sohail, G.M., Liu, K.-Y., Du, Q.-Z., Boateng, C.D., 2021. Study on brittleness templates for shale gas reservoirs-A case study of Longmaxi shale in Sichuan Basin, southern China. Petrol. Sci. 18 (5), 1370–1389. https://doi.org/10.1016/j.petsci.2021.09.030.
Yu, Q.L., Ranjith, P.G., Liu, H.Y., Yang, T.H., Tang, S.B., Tang, C.A., Yang, S.Q., 2014. A mesostructure-based damage model for thermal cracking analysis and application in granite at elevated temperatures. Rock Mech. Rock Eng. 48 (6), 2263–2282. https://doi.org/10.1007/s00603-014-0679-5.
Yu, Q., Yang, S., Ranjith, P.G., Zhu, W., Yang, T., 2015. Numerical modeling of jointed rock under compressive loading using X-ray computerized tomography. Rock Mech. Rock Eng. 49 (3), 877–891. https://doi.org/10.1007/s00603-015-0800-4.
Yu, Q., Liu, H., Yang, T., Liu, H., 2018. 3D numerical study on fracture process of concrete with different ITZ properties using X-ray computerized tomography. Int. J. Solid Struct. 147, 204–222. https://doi.org/10.1016/j.ijsolstr.2018.05.026.
Yu, H., Taleghani, A.D., Lian, Z., 2021. A new look at rock mechanical behavior from the meso-scale grain. J. Petrol. Sci. Eng., 108373 https://doi.org/10.1016/j.petrol.2021.108373.
Yue, Z.Q., Chen, S., Tham, L.G., 2003. Finite element modeling of geomaterials using digital image processing. Comput. Geotech. 30 (5), 375–397. https://doi.org/10.1016/S0266-352X(03)00015-6.
Zeng, L., Lyu, W., Li, J., Zhu, L., Weng, J., Yue, F., Zu, K., 2016. Natural fractures and their influence on shale gas enrichment in Sichuan Basin, China. J. Nat. Gas Sci. Eng. 30, 1–9. https://doi.org/10.1016/j.jngse.2015.11.048.
Zhang, Y., Wong, L.N.Y., 2018. A review of numerical techniques approaching microstructures of crystalline rocks. Comput. Geosci. 115, 167–187. https://doi.org/10.1016/j.cageo.2018.03.012.
Zhang, Y., Wong, L.N.Y., Chan, K.K., 2019. An extended grain-based model accounting for microstructures in rock deformation. J. Geophys. Res. Solid Earth 124 (1), 125–148. https://doi.org/10.1029/2018JB016165.
Zhang, J., Xu, J., Jiang, S., Tang, S., 2021. Quantitative identification and distribution of quartz genetic types based on QemScan: a case study of Silurian Longmaxi Formation in Weiyuan area, Sichuan Basin. Petroleum Research 6 (4), 423–430. https://doi.org/10.1016/j.ptlrs.2021.05.001.
Zhao, J., Zhang, D., 2020. Dynamic microscale crack propagation in shale. Eng. Fract. Mech. 228, 106906. https://doi.org/10.1016/j.engfracmech.2020.106906.
Zhao, Y., Sun, Y., Yuan, L., Xu, Q., 2020. Impact of nanopore structure on coal strength: a study based on synchrotron radiation nano-CT. Results Phys. 17, 103029. https://doi.org/10.1016/j.rinp.2020.103029.
Zhao, X., Jin, F., Liu, X., Zhang, Z., Cong, Z., Li, Z., Tang, J., 2022. Numerical study of fracture dynamics in different shale fabric facies by integrating machine learning and 3-D lattice method: a case from Cangdong Sag, Bohai Bay basin, China. J. Petrol. Sci. Eng., 110861 https://doi.org/10.1016/j.petrol.2022.110861.
Zhu, W.C., Tang, C.A., 2004. Micromechanical model for simulating the fracture process of rock. Rock Mech. Rock Eng. 37 (1), 25–56. https://doi.org/10.1007/s00603-003-0014-z.
Zhu, W.C., Liu, J., Yang, T.H., Sheng, J.C., Elsworth, D., 2006. Effects of local rock heterogeneities on the hydromechanics of fractured rocks using a digital-image-based technique. Int. J. Rock Mech. Min. Sci. 43 (8), 1182–1199. https://doi.org/10.1016/j.ijrmms.2006.03.009.
Zhu, J.B., Zhou, T., Liao, Z.Y., Sun, L., Li, X.B., Chen, R., 2018. Replication of internal defects and investigation of mechanical and fracture behaviour of rock using 3d printing and 3d numerical methods in combination with x-ray computerized tomography. Int. J. Rock Mech. Min. Sci. 106, 198–212. https://doi.org/10.1016/j.ijrmms.2018.04.022.
Zou, Y., Zhang, S., Ma, X., Zhou, T., Zeng, B., 2016. Numerical investigation of hydraulic fracture network propagation in naturally fractured shale formations. J. Struct. Geol. 84, 1–13. https://doi.org/10.1016/j.jsg.2016.01.004.